DEVELOPMENT OF MOLECULAR CONTRAST IN COHERENCE DOMAIN OPTICAL IMAGING

A Dissertation

by

QIUJIE WAN

Submitted to the Office of Graduate Studies of
Texas A&M University
in partial fulfillment of the requirements for the degree of

DOCTOR OF PHILOSOPHY

December 2011

Major Subject: Biomedical Engineering

Development of Molecular Contrast in Coherence Domain Optical Imaging

DEVELOPMENT OF MOLECULAR CONTRAST IN COHERENCE DOMAIN OPTICAL IMAGING

A Dissertation

by

QIUJIE WAN

Submitted to the Office of Graduate Studies of
Texas A&M University
in partial fulfillment of the requirements for the degree of

DOCTOR OF PHILOSOPHY

Approved by:

Chair of Committee,	Brian E. Applegate
Committee Members,	Alvin T. Yeh
	Javier Jo
	Jim Ji
Head of Department,	Gerard L. Cote

December 2011

Major Subject: Biomedical Engineering

ABSTRACT

Development of Molecular Contrast in Coherence

Domain Optical Imaging. (December 2011)

Qiujie Wan, B.S. Anhui University of Technology; M.S. Texas A&M University

Chair of Advisory Committee: Dr. Brian E. Applegate

Optical imaging has been developed quickly in the past decades because it has become an important research tool in biology, biochemistry, and biomedical sciences. Coherence domain optical imaging is one of the well developed optical imaging modalities, as it provides high resolution and long penetration depth. In this dissertation, we will report our work on development of molecular contrast in coherence domain optical imaging.

In order to image important molecules which are poor fluorophores, we developed a high resolution molecular imaging technique, pump-probe optical coherence microscopy (PPOCM), which does not rely on fluorescent tags. PPOCM is the fusion of Pump-Probe spectroscopy and optical coherence microscopy (OCM). We have demonstrated the prototype system on a fixed human skin sample containing a nodular melanoma. The results indicate that PPOCM can clearly provide strong contrast between the melanotic and amelanotic regions. This technique can be applied to early diagnosis of melanoma and the mapping of tumor margins during excision. It also can be extended to any biological chromophore with a known absorption spectrum and sufficient

concentration. In order to differentiate further multiple chromophores, we developed a spectrally resolved two color pump-probe Optical Coherence Microscopy (SRPPOCM). We showed the prototype system on a red hair and a black hair. Our preliminary results show that the SRPPOCM technique could provide a contrast between pheomelanin and eumelanin. This technique could be used potentially as a clinical tool for diagnosing different progression stages of melanoma. This technique could also be applied to differentiate other mixed chromophores.

Second harmonic optical coherence tomography (SHOCT) is non-linear high resolution optical molecular imaging modality which is widely used in non-centrosymmetric material. However, depth ambiguity is associated with SHOCT in tissue sample because forward generated second harmonic signal does not correctly report where the second harmonic signal is generated. We studied the feasibility of collecting the backward generated second harmonic signal from nanocrystals through a Second Harmonic Optical Coherence Tomography in Fourier domain. The preliminary result shows that we can collect backward generated second harmonic signal from nanocrystals which indicates that this technique could suppress the depth ambiguity.

DEDICATION

This dissertation is lovingly dedicated to my parents, husband and our daughter, for their support, sacrifice and love throughout my life.

ACKNOWLEDGEMENTS

I would like to thank my Ph.D. advisor, Dr. Brian Applegate. Throughout my doctoral studies, he provided encouragement, great advice and good guidance. What I have learned from him goes far beyond research methodologies and techniques. I am impressed by his focus and perseverance and passion. I owe him lots of gratitude for making my research life enjoyable and rewarding.

I would like to thank my committee members, Dr. Yeh, Dr. Jo and Dr. Ji, for their guidance and support throughout the course of this research.

I wish to express my warm and sincere gratitude to all my lab buddies in Laboratory for Optical and Molecular Imaging, Dr. Jesung Park, Dr. Nilanthi Warnasooriya, Ryan Shelton and Sebina Shrestha, for their friendship and help. They made the lab a convivial place to work.

Thanks also go to my friends, colleagues, the department faculty and staff for making my time at Texas A&M University a great experience. I also want to extend my gratitude to the National Institutes of Health, which supports our research projects.

Finally, thanks to my parents, husband and my daughter for their patience, encouragement and love.

NOMENCLATURE

OCT	Optical Coherence Tomography
OCM	Optical Coherence Microscopy
PPOCM	Pump-Probe Optical Coherence Microscopy
FWHM	Full width half maximum
SRPPOCM	Spectrally Resolved Pump-Probe Optical Coherence Microscopy
SHOCT	Second Harmonic Optical Coherence Tomography
TD-OCT	Time-domain OCT
FD-OCT	Fourier-Domain OCT
CARS	Coherent Anti-Stokes Raman Scattering
PSF	Point Spread Function
SNR	Signal to Noise Ratio

TABLE OF CONTENTS

LIST OF FIGURES

FIGURE Page

LIST OF TABLES

CHAPTER I

INTRODUCTION

Optical imaging has been developed quickly in the past few decades since laser was invented. In this chapter, we will briefly introduce some important optical imaging techniques and then discuss coherence domain imaging technique which is my research focus.

1.1 Current Optical Imaging Techniques

Currently tissue biopsy is the "gold standard" for the diagnosis and monitoring of numerous diseases. However, there are some disadvantages associated with this technique. First, tissue biopsy is an invasive method which involves the removal of tissues from a living object for examination. In addition, it doesn't show the dynamic information of the target molecules because the tissue sample is dead. Furthermore, additional artifacts or damage could be introduced into the tissue during the preparation process. Therefore, different high resolution optical molecular imaging modalities have been developed to overcome these issues with tissue biopsy.

This dissertation follows the style of Optics Express.

A number of high resolution optical molecular imaging modalities have been studied and developed to obtain molecular contrast. It has become a vital tool for understanding and measuring physiologically important biometrics on the cellular and subcellular level, e.g. collagen denaturation [1] and cellular metabolism [2]. In this chapter, we will discuss the most common and important imaging modalities: confocal fluorescence microscopy, two-photon fluorescence microscopy, second harmonic imaging, Coherent Anti-Stokes Raman Scattering (CARS) imaging, pump-probe based imaging, coherence domain optical imaging.

Prevailing high resolution molecular imaging modalities are based on fluorescence. Fluorescence microscopy has become an essential imaging tool in biology and biomedical science. It is used to image a molecule or a microstructure tagged with fluorescent agents. However, the technique of delivering the fluorescent agents to the desired target is very challenging, especially in the complicated organisms. Further application in humans is even more intricate because every tag and delivery system must be FDA approved.

The two most common forms of fluorescence microscopy are confocal microscopy and two-photon fluorescence microscopy. Fluorescence confocal microscopy provides a few advantages over conventional optical microscopy, including the elimination of background noise and ability to reconstruct 3-D images by sectioning. A pinhole is used in front of the detector in confocal microscopy to reject out of focus light in the samples. Fluorescence confocal microscopy can image up 100-200 μm deep [3, 4], and has been widely used in life science and material science. Two-photon

fluorescence microscopy is based on a nonlinear process of absorption of two photons. The first photon excites a molecule from ground state to a virtual intermediate state, the second photon excites it to a higher excited state and fluorescence light is emitted by relaxation to the lowest energy level. Two-photon fluorescence microscopy offers a few advantages, including reduced background signal and enhanced penetration depth. Two-photon fluorescence microscopy can image up to 1mm deep [5].

These techniques mainly rely on exogenous fluorescent tags because a large percentage of the biomolecular species have low intrinsic fluorescence. These tags may potentially interfere with the process under study or even cause toxic to the sample and also may increase experimental complexity [6, 7]. Photobleaching is another major issue with fluorescent tags in long-term measurement of biomolecular process. Therefore, researchers have developed a number of high resolution optical molecular imaging modalities which are not based on fluorescence, including second harmonic imaging, CARS imaging, pump-probe based imaging, and coherence domain optical imaging.

Second harmonic imaging is a powerful contrast mechanism in nonlinear imaging modality [8, 9 10]. Essentially, the image contrast is determined by the variations in a sample's ability to generate second harmonic signal. It has been used with great success to image highly ordered collagen. It can provide high resolution optical 3-D sectioning images for the samples because it only generates the second harmonic signal at the focal volume of the objective. Second harmonic generation (SHG) doesn't involve the excitation of molecules and therefore the molecules do not undergo the

effects of phototoxicity or photobleaching. The choice of excitation wavelength of SHG is flexible because it is a non-resonant process. However, SHG technique requires non-centrosymmetric structure which limits its applicability.

Second harmonic imaging also can combine with other imaging techniques to create the new imaging modalities, such as second harmonic optical coherence tomography (SHOCT) and second harmonic optical coherence microscopy (SHOCM). SHOCT is the fusion of coherence gating of OCT with second harmonic generation while SHOCM is the fusion of coherence gating of OCM with second harmonic generation. Since the wavelength of second harmonic photons is the exact half of incident photons, the images could be background free. SHOCT can provide strong molecular contrast and high resolution images for non-centrosymmetric tissues. Jiang and coworkers have first demonstrated the images obtained via a SHOCT from collagen fibrils organization in rattail tendon [11].

Coherence Anti-Stokes Raman Scattering imaging has CARS imaging is a label free and nonlinear technique that provides contrast based on the molecular vibrations [12]. CARS involves using two laser pulses at different wavelengths. When the difference in frequency between the two pulses matches the frequency of a Raman active molecular vibration, a strong anti-Stokes resonance signal is generated in the sample. The anti-Stokes signal can be easily separated from fluorescence signal since it is blue-shifted from the two laser wavelengths. CARS can provide three-dimension images by sectioning due to the nonlinear process. This technique has been used in metabolite and drug imaging and tumor identification [13].

Coherence domain optical imaging is one of the well developed optical imaging modalities as it provides high resolution and long penetration depth. The prevailing optical imaging modalities based on coherence domain are optical coherence tomography (OCT) and optical coherence microscopy (OCM). OCT and OCM have been used in clinical examination and biology, biochemistry, and the biomedical sciences research. Fujimoto and coworkers first demonstrated a femtosecond ranging result to measure corneal thickness and the depth of the stratum corneum and epidermis using OCT [14]. OCT is based on low coherence interferometry [15, 16, 17]. Currently, OCT offers axial resolution from 1- 15 μm and penetration depth up to ~ 2mm [18]. OCT has become a clinical tool in ophthalmology [19]. OCM is a special adaption of OCT for better lateral resolution in highly scattering tissues [20]. The major difference between OCT and OCM is that OCM uses an objective with high numerical aperture (NA) whereas OCT employs an objective with low NA. Thus, OCM provides better lateral resolution images than OCT. However, the depth of focus in OCM is shorter than OCT because the high NA objective is used. Both OCT and OCM are powerful techniques and can be combined with other imaging modalities.

Pump-probe absorption spectroscopy is a well developed modality in molecular physics for measuring the spectrum and dynamics of molecular species which cannot generate fluorescence or are poor fluorophores. A pump beam induces molecular population change of the sample and a probe beam interrogates the change. It has been adapted for molecular imaging to provide molecular contrast due to resonant light absorption in biological tissues. Rao and coworkers first demonstrated an adapted pump-

probe spectroscopy to OCT (PPOCT) to show a transient absorption of a triplet state of the dye Methylene Blue [21]. Warren and coworkers have reported a nonlinear microscopy technique, which is transient absorption combined with pump-probe spectroscopy [22]. They were able to image hemoglobin in transmission but at a limited imaging depth. The same group also demonstrated images of melanin with their nonlinear microscopy system [23]. A ground state recovery pump-probe OCT (gsrPPOCT), which combines pump-probe spectroscopy with Optical Coherence Tomography (OCT) has been reported by Applegate and coworkers [24]. They imaged several endogenous chromophores including hemoglobin in the efferent filament arteries of an adult zebrafish. They were also able to measure the ground state recovery time of hemoglobin and rhodamine 6G, respectively, and separate the signal contributions from their mixture. This imaging provides 10-20 μm lateral resolution and 5-10 μm axial resolution, which is adequate to image micron scale morphology of living tissues.

1.2 Coherence Domain Optical Imaging

1.2.1 Introduction of Interferometry

Let's consider an interferometry system before we discuss OCT. The electric field in a light wave can be written as equation (1-1). We only consider z-direction because the sample beam and reference beam copropogate and thus they won't interfere along x or y. In the other words, the interference output in x or y direction is zero. When two coherent beams combine together their fields can produce interference. The output of the interferometer is the summation of the two electric fields, the reflected

beam from reference and reflected beam from the sample. The detector measures the intensity of the beam, which is proportional to the square of the electromagnetic field, as shown in equation (1-2) [18].

$$E_t(t) = E_i \cos\left(2\pi\nu t - \frac{2\pi}{\lambda} z\right) \tag{1-1}$$

$$I_0(t) \sim \frac{1}{4}|E_R||E_R| + \frac{1}{4}|E_s||E_s| + \frac{1}{2}E_R E_s \cos\left(2\frac{2\pi}{\lambda}\Delta l\right) \tag{1-2}$$

l_R: the distance that light travels from beam splitter to reference mirror; I_S: the distance in the light travels from the beam splitter to the sample; $\Delta l = l_R - l_S$. The pathlength in the reference arm changes when the position of the reference mirror is changed, and therefore interference may occur. A simple schematic interferometry is shown in figure 1.1. A beamsplitter splitters the light source into reference arm and sample arm and recombines the reflected beams from the mirror in the reference arm and from the sample in the sample arm, respectively. The mixed beam is then directed onto a detector. The bandwidth of the light spectrum is inversely proportional to coherence length.

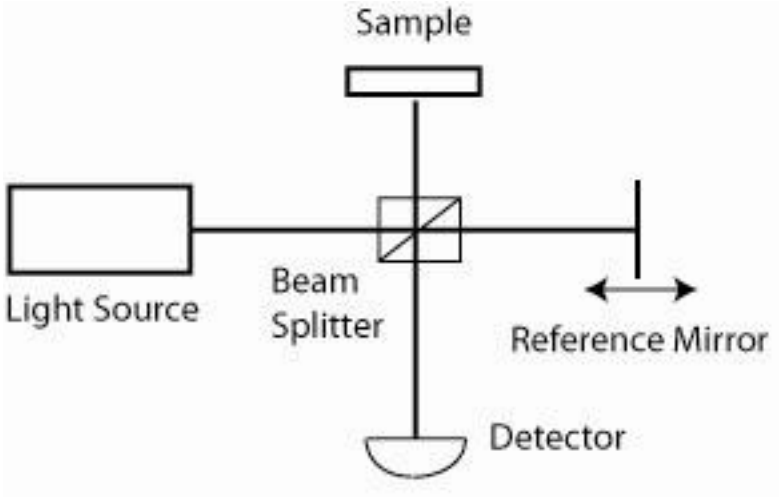

Figure 1.1 A simple schematic interferometry setup. It is based on a Michelson interferometer.

For an interferometry system interference signal only can be measured when the difference of path length between sample and reference arm is smaller than the coherence length. For biological application, one would use the shot coherence length light source to measure absolute distance or dimension of the sample. The reason is that axial resolution is equivalent to the coherence length. The better axial resolution can be achieved if a shorter coherence length light source is used.

1.2.2 Optical Coherence Tomography

People have developed OCT and OCM based on the Michelson interferometer. A general schematic OCT system is shown in Figure 1.2. In an OCT system, a 2X2 fiber coupler evenly splits the incident power of a low coherence source into a reference arm and sample arm. In the reference arm light exits the fiber and passes through an optical delay and then is reflected back into the fiber. In the sample arm light exits the fiber and is scanned by a scanning mechanism, usually a galvanometer, and then is focused onto the sample by an objective with low numerical aperture (NA). The scanning system is usually controlled by a computer. The backscattered or reflected light from the sample is combined with the reflected reference arm in the fiber coupler and then the mixed light is directed into the detection system by the fiber coupler.

The signal is processed into a depth resolved reflectivity profile, termed as A-scan (A-line) while the sample is at the focal volume and sample beam is at a fixed lateral position. A cross sectional image, termed as B-scan, can be obtained by multiple

scanning of A-scan along the lateral position. In addition, a three-dimension OCT image can be obtained by multiple B-scan.

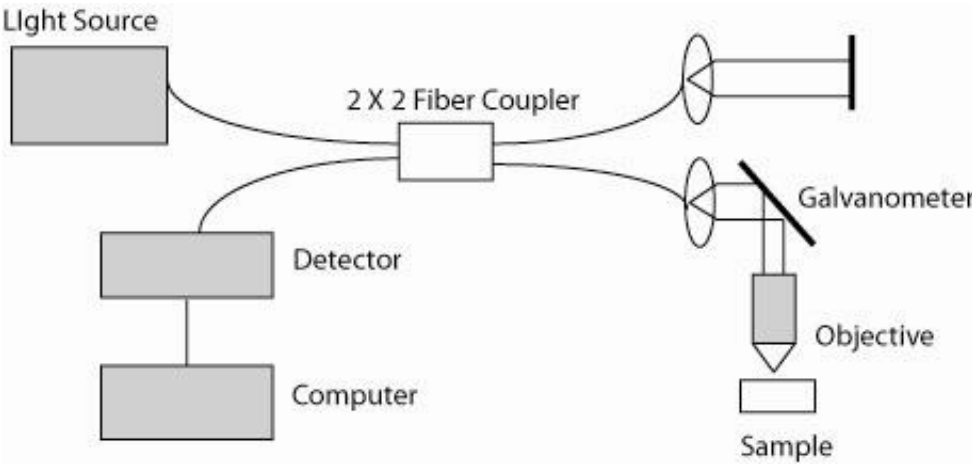

Figure 1.2 A general schematic OCT system.

For an OCT/OCM system the axial and lateral resolution are independent if we assume that axial resolution of OCM system is dominated by coherence gate. The axial resolution is determined by the coherence length of the light source. The axial resolution Δz can be written in the following form, assuming a Gaussian spectrum of the light source [18].

$$\Delta z = \frac{2ln2}{\pi}\left(\frac{\lambda^2}{\Delta\lambda}\right) \tag{1-3}$$

Δλ is the full width half maximum (FWHM) of power spectrum;

λ is the center wavelength of light source;

Δz is the axial resolution, the FWHM of the autocorrelation function.

According to this formula we can see that the axial resolution is inversely proportional to the bandwidth of the light source. Therefore, a broad bandwidth source is needed in order to obtain a high axial resolution image. The lateral resolution Δx is determined by the focusing optics of the system, as shown in equation (1-4) [18].

$$\Delta x = \frac{4\lambda}{\pi}\frac{f}{d} \tag{1-4}$$

d is the beam diameter of the collimated beam on the objective,

f is the focal length of the objective.

Another important parameter is depth of focus, b, which is two times the Rayleigh range:

$$b = \frac{\pi \Delta x^2}{2\lambda} \tag{1-5}$$

Thus, it is a trade off relationship between depth of focus and lateral resolution. The depth of focus decreases if the lateral resolution increases. Figure 1.3 shows the relationship between lateral resolution and depth of focus with low NA and high NA, respectively.

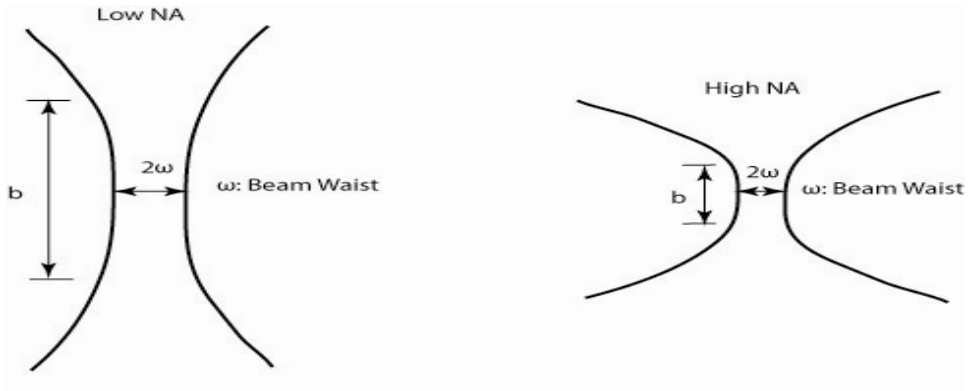

(a) (b)

Figure 1.3 Focusing limit for OCT. (a) Low resolution and long depth of focus for high NA. (b) High resolution and short depth of focus for low NA.

There are two types of OCT systems, one is time domain OCT (TD-OCT) and another is termed as Fourier-domain OCT (FD-OCT). In TD-OCT, the location of the coherence gate changes when the mirror in reference arm scans at a certain frequency. In FD-OCT the reference mirror is in a fixed position. For a TD-OCT, both lateral scanning and axial scanning have to be performed, whereas only the lateral scanning is performed in FD-OCT. FD-OCT was first reported by Fercher and coworkers which can generate the A-lines without scanning the reference mirror and thus greatly increases imaging speed [25]. In FD-OCT, all scatters in an A-line are simultaneously measured and contribute to the interference signal. An A-line image can be acquired by Fourier transform of the spectrum of the interferogram. In general, two types FD-OCT have been well developed; one is spectrometer based which employs a spectrometer as the detector in conjunction with a high dynamic range CCD camera, and another one is swept source based which utilizes a swept laser with narrowband wavelength as the source. It has been shown that the sensitivity of Fourier-domain OCT is better than time-domain OCT because all scatters in an A-line are measured simultaneously [26].

1.2.3 Optical Coherence Microscopy

General OCT offers a non-invasive modality to image material and biological tissue with high resolution of 1-15 μm [18]. Higher lateral resolution images are needed in some research field. A traditional OCT can't provide cellular and subcellular imaging due to the usage of low NA objective. In contrast, OCM can provide cellular and

subcellular imaging due to the usage of high NA objective. However, the depth of focus of OCM is shorter than that of OCT.

In this dissertation OCM refers to coherence-gated confocal microscopy to improve lateral and axial resolution. Confocal microscopy has been widely used to image thin biological tissue. It employs a pin hole, which serves as a spatial gate to reject light from the outside of focal plane. However, confocal microscopy is not able to reject multiple scattered light, which makes the image blur. Figure 1.4 illustrates an experimental source autocorrelation function of an OCM system as well as a confocal axial response for a planar mirror sample [20]. In this experiment, the autocorrelation function was obtained by scanning a mirror through the focal region and the confocal axial response was obtained by scanning a mirror through the focal region while blocking the reference arm. As shown in figure 1.4, the axial response of the confocal microscope dominates the axial resolution when the mirror is close to the focal plane. When it moves away from the focal plane the coherence gate dominates the axial resolution which means it will reject the scattered light that is not able to be rejected in confocal microscope (can be seen better in logarithmic scale). In other words, the coherence gate can reject multiple scattered light. Similarly as OCT, there are time domain OCM (TD-OCM) and Fourier domain OCM (FD-OCM). In this dissertation, we will focus on TD-OCM. The well-known signal to noise ratio (SNR) is given by [27]

$$SNR = \frac{\rho S_{TDOCT} R_S}{2eB_{TDOCT}} \tag{2-6}$$

e is the electronic charge;

ρ is the detector responsivity;

S_{TDOCT} is the instantaneous source power;

R_S is the sample reflectivity;

B_{TDOCT} is the electronic detection bandwidth system.

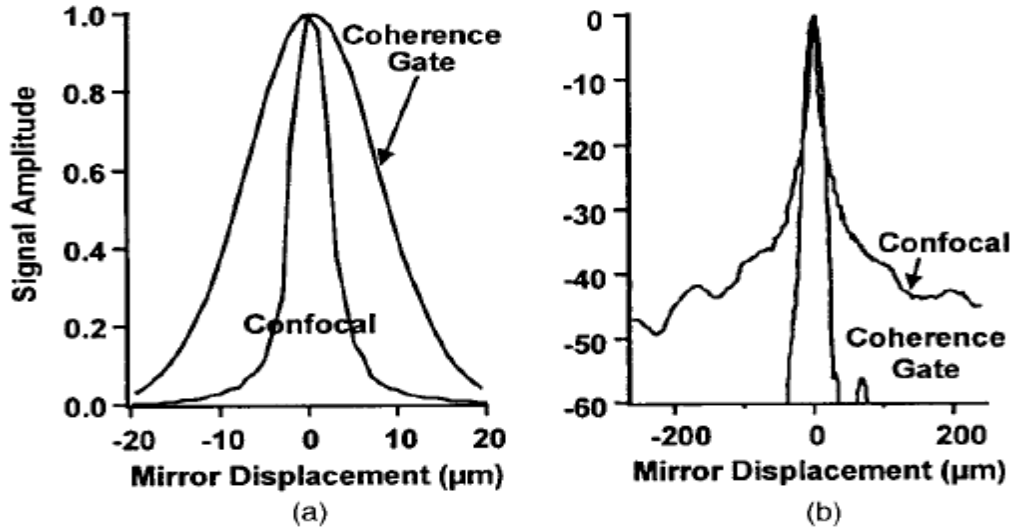

Figure 1.4 Experimental confocal axial response and autocorrelation function of an OCM system with a 0.65 NA objective. (a) Linear scale; (b) logarithmic scale [20, © 1996 IEEE].

1.3 Pump-Probe Spectroscopy

Pump-probe absorption spectroscopy is a well established modality in molecular physics for measuring the spectrum and dynamics of molecular species which are poor fluorophores. The relaxation dynamics of DNA after absorption of UV light has been studied using pump-probe absorption spectroscopy [28]. The foundation of the technique is the detection of transient changes in absorption induced by the pump beam. The energy diagram for a pump probe experiment is shown in figure 1.5. Two laser pulses,

the pump and probe, temporally separated by a delay time. The probe pulses drive molecules from the ground state to the excited state when pump beam is off. When pump is on some molecules are driven from the ground state to the excited state due to pump pulses and some molecules are driven from the ground state to the excited state due to probe pulses. The absorption due to probe beam is weaker when the pump is on as compared to when the pump is off. Thus, the intensity of the probe radiation is stronger when the pump is on as oppose to when the pump is off due to the reduced probability of absorption and the increased probability of stimulated emission.

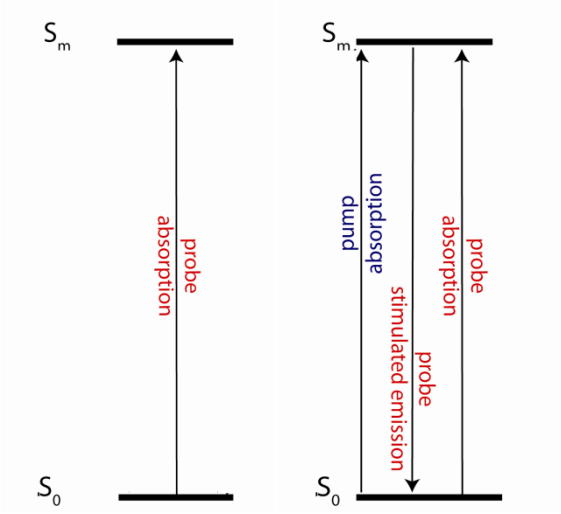

Figure 1.5 Energy diagram for a pump probe experiment. S_0 stands for the ground state and S_m stands for the excited state.

The pump-probe technique we employed in this dissertation was to measure a change in the ground state population of the target chromophores. Applegate and coworkers have shown that the strategy will yield better sensitivity than the pump-probe

techniques which measure excited state population changes [29]. Similarly, it also requires less *a priori* knowledge of the absorption spectrum of the target chromophore.

The ground state recovery time is the time needed for the molecules excited by the pump pulse to spontaneously return to the ground state, which is a specific parameter of a molecular chromophore and its local environment. The ground state recovery time can be obtained by measuring the magnitude of the transient absorption while varying the delay time between pump and probe as shown in figure 1.6. Ground state recovery time provides a means to differentiate among multiple chromophores.

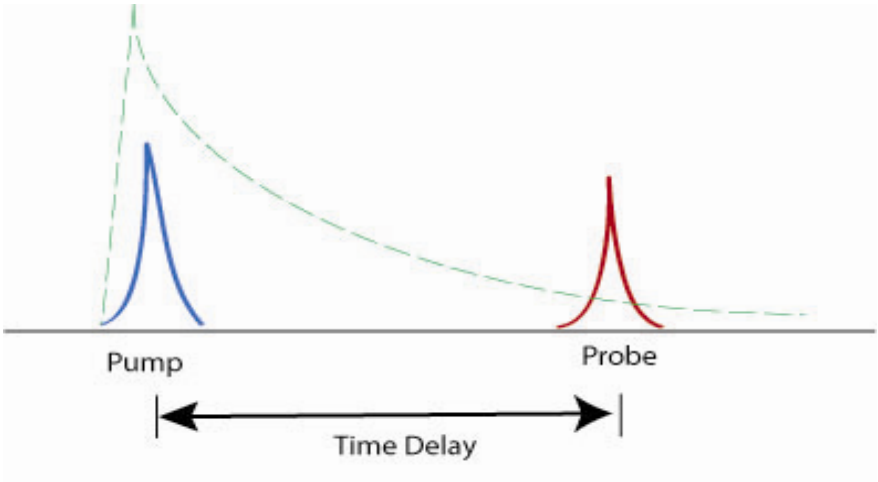

Figure 1.6 A schematic diagram of mapping the ground state recovery time by varying the time delay between pump and probe.

Another distinct molecular property is the magnitude of the transient absorption spectrum. The magnitude of the transient absorption can be mapped out by varying the pump wavelength. Any measured shifts in the peaks of the absorption spectrum may also provide clues to the local environment of the chromophore, for instance pH. Thus,

we can use the transient absorption spectrum to differentiate the multiple chromophores in a mixture.

1.4 Importance of Research

As we discussed earlier, fluorescence based imaging are not able to image a large number of important molecules that do not generate fluorescence or are poor fluorophores. SHG imaging requires noncentro-symmetric sample which limits its applicability. CARS imaging can potentially show high molecular specificity but the imaging depth is limited as multi photon fluorescence microscopy. Therefore, it is desirable to develop another high resolution molecular imaging which can provide molecular contrast. In order to achieve this goal, we combined pump-probe spectroscopy with OCM to yield Pump-Probe Optical Coherence Microscopy (PPOCM). We hope this technique can provide micron scale morphology at cellular and subcellular level. OCM is the combination of low coherence interferometry with confocal microscopy. In general confocal microscopy, the backscattered light from the sample is filtered by the confocal gate. Only backreflected light from the sample within the focal volume of objective can reach the detector since a pinhole is often used in front of the detector which enforces single spatial mode. When combined with low coherence interferometry, coherence gate is employed to yield scattering based images at depths better than the standard confocal microscopy [30]. Pump-probe spectroscopy is a well developed technique which can be applied to measure the spectrum and dynamics of molecules that are not accessible to fluorescence based imaging. When coupled with a

pump-probe spectroscopy, a molecular dependent gate will be added and enable the simultaneous acquisition of a molecular image as well as scattering based image. We will describe the PPOCM in Chapter II in details.

In order to further differentiate multiple chromophores, we developed a spectrally resolved two color pump-probe Optical Coherence Microscopy (SRPPOCM). Resolving the spectral dependence of PPOCM signal at the pump wavelengths can map out the absorption spectrum and, thus, provide improved specificity for particular chromophores. The improved specificity may then be used to differentiate between related chromophores like pheofmelanin and eumelanin. The concentration ratio of pheomelanin to eumelanin could potentially be used to diagnosis the progression stage of skin cancer due to melanoma [31]. We will introduce SRPPOCM in Chapter III in details.

SHOCT combines second harmonic generation with coherence gate to obtain images for noncentro-symmetric samples with molecular contrast. However, depth ambiguity is associated with SHOCT in tissue sample because the depth information is not clearly resolved by collecting the forward generated second harmonic signal. Considering the second harmonic signal generated at a certain depth in the tissue, if the second harmonic photons are immediately backscattered, the detected SHG signal will correctly report the depth at which the signal is generated. However, if the SHG light still propagates deeper into the tissue before being backscattered, the forward generated second harmonic won't report the correct depth information. Therefore, the measured SHG signal will not report the correct depth profile, and currently no algorithm is

available to correct the ambiguity. We studied the feasibility of collecting the backward generated second harmonic signal from nanocrystals through a Second Harmonic Optical Coherence Tomography in Fourier domain. This work will be described in Chapter IV.

CHAPTER II

NEAR DEGENERATE PUMP-PROBE OPTICAL COHERENCE MICROSCOPY*

The work described here represents our efforts in building a high spatial resolution molecular optical imaging microscopy for poorly fluorescing biomolecular species. In order to achieve this goal we have combined pump-probe spectroscopy with OCM to yield PPOCM. In this chapter, we will discuss this technique in detail.

2.1 Introduction of PPOCM

Currently high resolution optical molecular imaging plays a very important role as a research tool for biology, biochemistry, and the biomedical sciences. As we discussed in previous chapter, there are some drawbacks associated with the fluorescence based imaging, the prevailing high resolution optical molecular imaging modality. Exogenous tags are needed to probe these poorly fluorescing biomolecular species. Therefore, it is desirable to develop another high resolution molecular imaging which can provide molecular contrast.

---

* Part of this section is reprinted with permission from "Multiphoton coherence domain molecular imaging with pump-probe optical coherence microscopy" by Qiujie Wan and Brian E. Applegate 2010, *Optics Letters,* **35**, 532-534 Copyright 2010 by Optical Society of America.

2.1.1 PPOCM Signal in Theory

Applegate and coworkers have derived the equations which describe signal to noise ratio (SNR) of a gsrPPOCT system [32]. gsrPPOCT is the fusion of degenerate pump-probe spectroscopy with OCT. Signal to noise of the gsrPPOCM and PPOCM are essential the same. And thus we can use the same equation to describe SNR of PPOCM. A summary of this work is listed below. The SNR of the gsrPPOCT for a two-level molecular model system is given by [32]:

$$SNR = \frac{R\rho\Delta t}{2e} e^{-\sigma_1 (N_1(t) - N_2(t))z} P_{pr} \tag{2-1}$$

$$\text{with } N_1(t) - N_2(t) = N_1^0 \left(1 - \exp\left(-\frac{2\sigma_1 \lambda_{pu} P_{pu} \cos^2(\omega t)}{hc\pi w_0^2} \right) \right) \tag{2-2}$$

$$\text{and } SNR \approx \frac{R\rho\Delta t}{2e} \left(\frac{\sigma_1^2 z N_1^0 \lambda_{pu} P_{pu}}{hc\pi w_0^2 f_0} \right)^2 P_{pr} \tag{2-3}$$

where R is the sample reflectivity, ρ is the detector responsivity, P_{pr} is the sample arm power in the OCT interferometer, t is the integration time, e is the electron charge, f_0 is the laser pulse repetition rate, $N_1(t)$ and $N_2(t)$ are the time dependent ground and excited state populations integrated over the pump pulse duration, N_1^0 is the ground state population before interacting with the pump laser, σ_1 is the absorption cross section, z is the absorption path length, λ_{pu} is the pump wavelength, P_{pu} is the average pump power, ω is the pump modulation frequency, h is Planck's constant, c is the speed of light, and w_0 is the focal spot radius. The approximation is a result of assuming weak absorption of the pump and probe beams where the exponential function may be approximated by the

first two terms of its Taylor series expansion. Equation (2-2) has been shown to be consistent with experimental measurements using rhodamine 6G [24]. The gsrPPOCT signal is inherently pathlength (z) and reflectivity (R) dependent as shown in equation (2-3).

2.1.2 Point Spread Function

The point spread function (PSF) describes the response of an imaging system to point source or point object. In general, it refers to the impulse response of a focused optical system.

Image formation in PPOCM follows from the three gates, coherence gate, confocal gate and molecular dependent gate, which is introduced from pump-probe spectroscopy. In general confocal microscopy, the backscattered light from the sample is filtered by the confocal gate. Only backreflected light from the sample within the focal volume of objective can reach the detector as a pinhole is often used in front of the detector which enforces the single spatial mode. When OCM combines with low coherence interferometry, coherence gate is employed to yield scattering based images at depths better than the standard confocal microscopy [30]. When OCM couples with a pump-probe spectroscopy, a molecular dependent gate will enable the simultaneous acquisition of a molecular image as well as a scattering based image.

The coherence gate and the confocal gate combine to form the point spread function (PSF) of a typical OCM system. The coherence gate only contributes in the axial dimension (z) and is given by $PSF_L(z) = \exp\left(-\frac{z^2 4\ln 2}{(\Delta z)^2}\right)$, where Δz is the full width

at half maximum of the PSF. We have assumed a Gaussian source spectrum. Δz is the coherence length of the source which is related to the source center wavelength and bandwidth by $\Delta z = \frac{2\ln 2}{\pi}\frac{\lambda_0^2}{\Delta\lambda}$, where λ_0 is the center wavelength and $\Delta\lambda$ is the source full width at half maximum. The confocal gate contributes in both the axial and lateral dimensions. The confocal PSF, following Sheppard and Gu [33], is given by $PSF_C(z,r) = I(r,z)^2$, where $I(r,z) = \left| 2\int_0^1 J_0(kr\sin\alpha, q)\exp\left(\tfrac{1}{2} i 4kz\sin^2(\alpha/2)q^2\right)dq \right|^2$ and sin α is the numerical aperture of the objective. If we take the product of the two we will have:

$$PSF_{OCM}(z) = \exp\left(-\frac{z^2 4ln2}{(\Delta z)^2}\right) I(z,r)^2 \tag{2-4}$$

If we have a long coherence length equation (2-4) becomes the PSF of a confoal microscope. Similarly, if we have a long depth of focus equation (2-4) becomes the PSF of OCT.

The molecular gate in PPOCM is due to the overlap of the pump and probe beams. Following Dong and coworkers work [34], if there is no confocal gate the PSF due to the overlap of the pump and probe can be expressed:

$$PSF_{P-P} = I(r,z)I'(r',z') \tag{2-5}$$

where the prime indicates the pump beam and we assume that the chromophores are not saturated. If there is a confocal gate the PSF is then be written:

$$PSF_{P-P,C} = I(r,z)I'(r',z')I(r,z)\,. \tag{2-6}$$

Adding the coherence gate we will have the PSF equation in PPOCM,

$$PSF_{PPOCM}(r,z) = \exp\left(-\frac{z^2 4\ln 2}{(\Delta z)^2}\right) I(r,z)^2 I'(r',z') . \tag{2-7}$$

The spatial resolution of PPOCM may exceed that of the base OCM system. It is mainly determined by the focusing of pump beam. Figure 2.1 illustrate the relationship among these gates. If the pump beam is unfocused, PSF_{PPOCM} is equivalent to PSF_{OCM}. If the saturation of the transition is presented, PSF_{PPOCM} will approach PSF_{OCM}. We emphasize that even if the transition is completely saturated by the pump the spatial resolution will not below that of the base OCM system. On the other words, if the spatial resolution is only determined by the molecular gate the maximum signal would be accompanied by a deterioration of the spatial resolution.

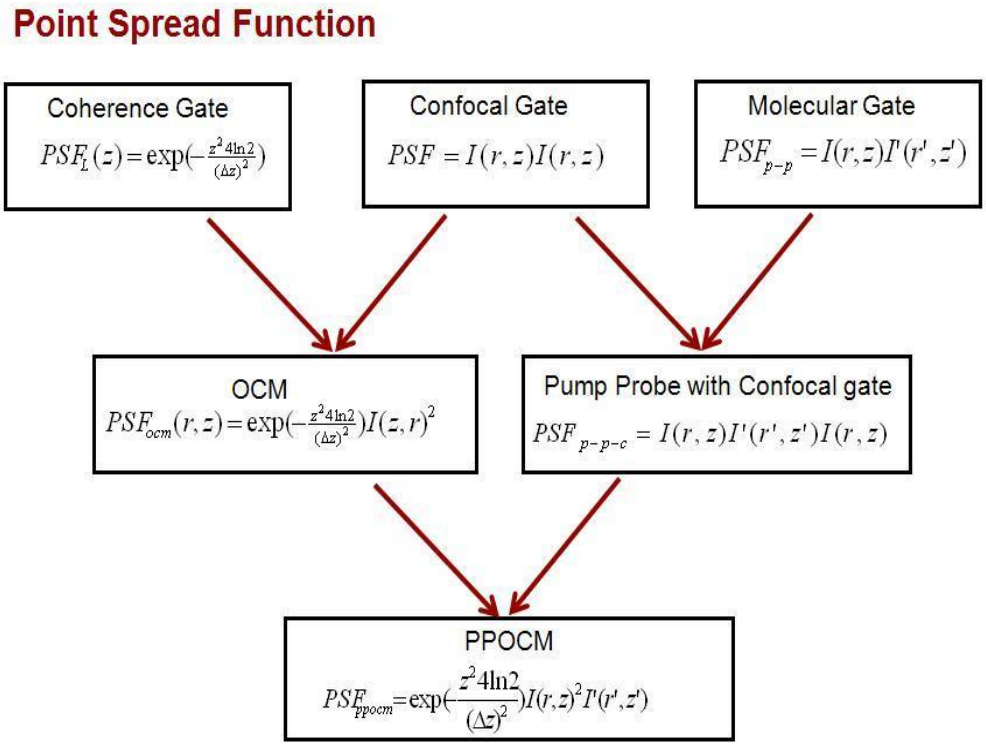

Figure 2.1 Schematic diagram of the point spread function of different gate. The PSF is determined by coherence gate and confocal gate in OCM. The PSF is determined by coherence gate and confocal gate and molecular gate in PPOCM.

Based on the relationship between Δz and $\Delta\lambda$ it would appear that we may arbitrarily improve the PPOCM axial resolution by increasing the probe bandwidth, similar to OCM. There are two confounding factors which restrict this relationship. First, probe bandwidth larger than the bandwidth of the transition being probed will not contribute to the PPOCM resolution because the additional bandwidth will not be modulated by the pump. Second, while the pump-probe overlap restricts the interaction region to approximately twice the Rayleigh range, subresolving that region by decreasing the source coherence length leads to an ambiguity in the spatial position where the absorption occurs. The ambiguity arises because absorption is an integrative process in pathlength, hence light reflected at any given depth necessarily reports attenuation from all shallower depths. The "ideal" probe would have a center wavelength and bandwidth closely matching the peak of the chromophore absorption spectrum and a coherence length greater than or equal to twice the Rayleigh range of the objective lens.

2.2 Materials and Methods

2.2.1 Optical Setup

Melanin was chosen as the initial target chromophore for our PPOCM system. Melanin is one of the most common chromophores in the human body. Different forms of melanin play important roles in the brain, ear, eyes, and skin. We could use this imaging technique as a tool to investigate and potentially diagnose melanoma, a particularly aggressive cancer. Melanoma is the most common form of skin cancer.

The optical system is shown schematically in Figure 2.2 [35]. The source was a tunable (680-1080 nm) 140 fs Ti:Sapph laser with a pulse repetition rate of 80 MHz. Approximately 250 mW of 800 nm light was launched into a 6.5 cm length of polarization maintaining high NA single mode fiber. We used the shortest practical fiber length that could be used in the fiber launching system in order to minimize the temporal broadening of the pulse. A polarizer was used to remove the center of the spectrally broadened pulse (figure 2.3 A [35]) and thus yield the bimodal spectrum shown in figure 2.3 B [35]. The short wavelength band was utilized as the pump and the long wavelength band was utilized as the probe. The setup of probe part is based on a Mach-Zehdner design. The coherence length is about 50 μm. A Piezoelectric Transducer (PZT) in the reference arm was driven at resonance (57.25 kHz) by a sine wave, which is the carrier frequency for the interferometric signal. The optically chopper modified the pump beam at 3.4 kHz. The pump beam passed through an optical delay line which rotated the polarization by 90 degrees. The pump was combined with the probe in the sample arm of the interferometer by using a polarizing beam splitter. The co-propating pump and probe were focused onto the sample using a 0.8 NA water immersion objective which provided sub 0.5 μm lateral resolution and a measured ~2 μm axial (confocal gate) resolution. The polarizing beam splitter prevented stray pump light from entering the detector. A 2X2 (50/50) single-mode fiber coupler served as the beamsplitter as well as the confocal pinhole in the Mach-Zehdner interferometer. The light was sent to a 125 kHz dual balanced detector by two outputs of the fiber coupler. The detector signal was digitized using a PC board and processed with custom Labview code. En face imaging was

accomplished by translating the sample using a high precision translation stage with computer controlled actuators. The measured SNR of the OCM system was 122 dB, with 5 dB offset from the shot-noise limit of 127 dB.

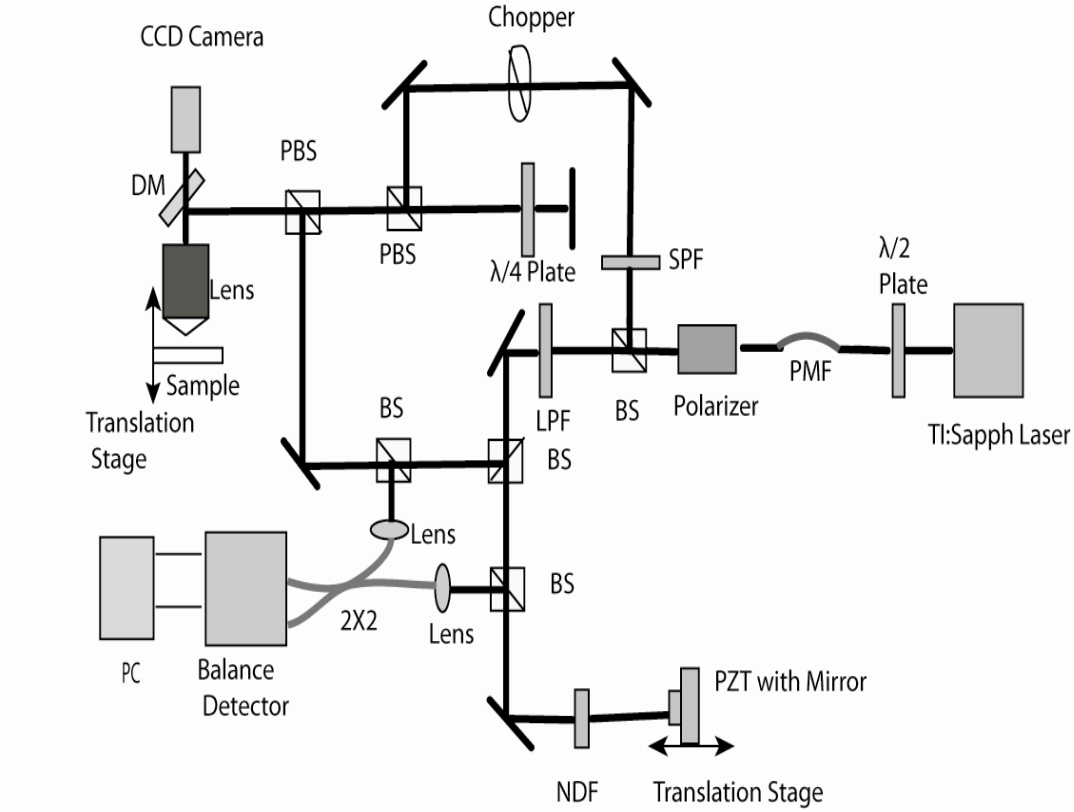

Figure 2.2 Schematic diagram of the pump-probe optical coherence microscope. Abbreviations, PMF: high NA polarization maintaining single mode fiber. Obj: objective; BS, beam splitter; PBS; polarized beam splitter; LPF, long pass filter; SPF, short pass filter; DM, dichroic mirror, 2X2; 2X2 50:50 fiber [35].

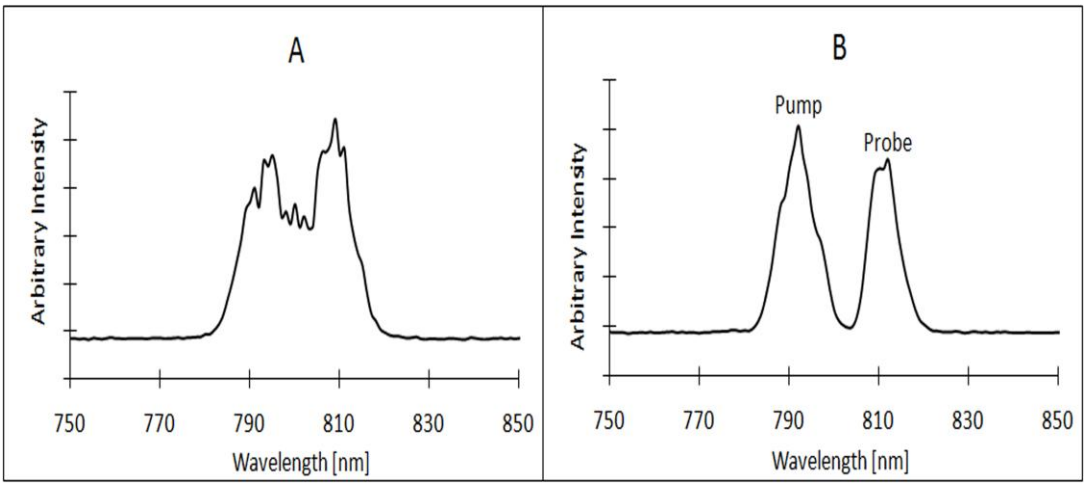

Figure 2.3 Representative source spectrums. A) Representative source spectrum after exiting the PMF. B) Representative source spectrum after the polarizer. The short wavelength band was used as the pump and the long wavelength band the

2.2.2 Modulation of PZT

PZT is often used for phase modulation in reference arm of OCM. It is inexpensive and convenient. However, temperature shift or physical variation can cause phase shift of the interferometric signal. In order to address this issue Hoeling and coworker has developed an algorithm to suppress the phase shift [36].

The output intensity of the interferometer it interference term can be written as:

$$I_0(t) = I_{DC} + I_0 \cos\left(2\frac{2\pi}{\lambda}\Delta l\right) \tag{2-8}$$

where λ is the wavelength of incident light;

I_{dc} is the DC component of the output intensity;

λ is the wavelength of probe beam;

Δl is the pathlength difference between sample arm and reference arm.

In order to eliminate the huge DC term we modulate the PZT with sinusoid wave and only measure the interference term (AC term). The AC term is given by [36]

$$I = I_0 \cos(\alpha \sin \omega t + \phi) \tag{2-9}$$

where ω is modulation frequency;

ϕ is the phase;

$I_0 = 2\sqrt{I_{ref} I_{sample}}$, where I_{ref} I_{sample} are the intensities returned from reference and sample arm, respectively.

$\alpha = \frac{4\pi d_0}{\lambda}$, it is related to the displacement amplitude of PZT, d_0 (peak-to-peak of d_0 =0.25λ) is the amplitude the sinusoid wave which is used to drive PZT.

The output fringe is a function of the phase. Figure 2.4 (a) shows the displacement of PZT. The peak-to-peak displacement is 0.25λ [36]. Figure 2.4 (b) and 2.4 (c) show the interference term of output fringe signal at ϕ=0 and ϕ=90, respectively. If we take Fourier transform of the two signals we will obtain two different outputs at fundamental frequency and different outputs at second harmonic frequency. In the other words, the interferometer output is varied due to random phase shift. To address this issue Hoeling and coworker have developed an algorithm which will be covered in next section.

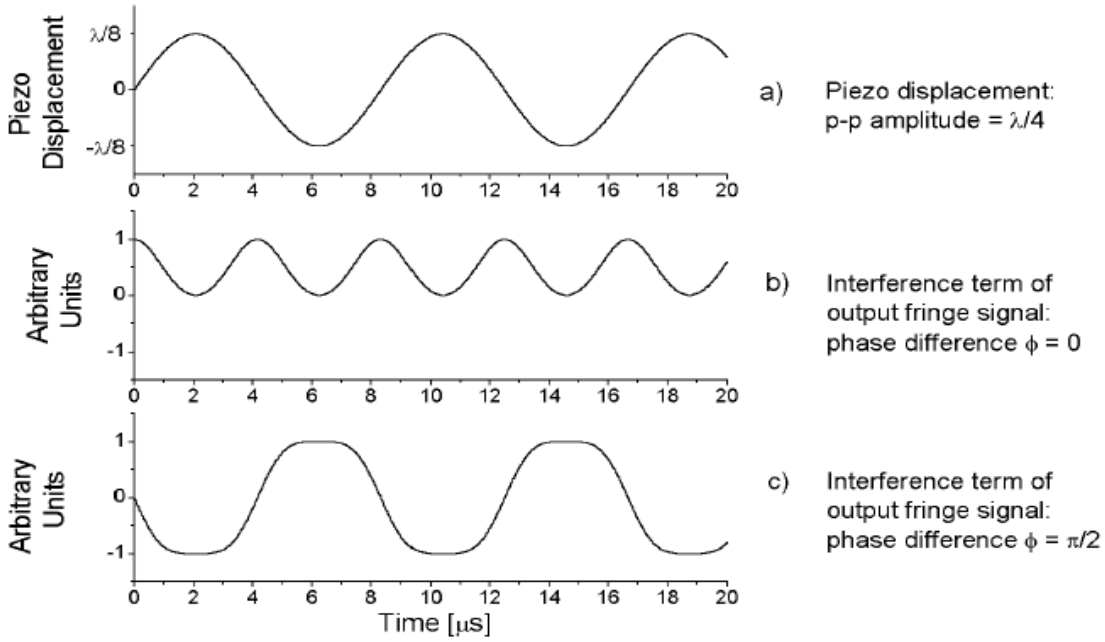

Figure 2.4 Output fringe signal as a function phase [36].

2.2.3 Signal Process

The extraction of the interferometric signal was based upon the algorithm presented in reference [36]. The desired signal (S_{OCM}) was the square root of the sum of the power at the pzt fundamental modulation frequency (P_1) and the 2nd harmonic (P_2), $S_{OCM} = \sqrt{P_1 + P_2}$ as shown in figure 2.5. The power of P_1 and P_2 are given (2-10) and (2-11) respectively.

$$P_1 = 2I_0^2 J_1^2(\alpha) sin^2\phi \tag{2-10}$$

$$P_2 = 2I_0^2 J_2^2(\alpha) cos^2\phi \tag{2-11}$$

where J_1 and J_2 are the first and second order Bessel functions. When $J_1^2(a) = J_2^2(a)$, P_1+P_2 is independent of ϕ. The reference has shown that S_{OCM} as calculated above was

independent of the phase of the interference signal if the amplitude of the pzt motion was 0.84 of a fringe. When the pump causes changes in probe signal there will be sidebands on P_1 and P_2 at +/- the pump modulation frequency. The PPOCM signal can be written as $S_{PPOCM} = \sqrt{P_{1-} + P_{2-}} + \sqrt{P_{1+} + P_{2+}}$, where the + and – subscripts indicate the plus and minus sidebands, respectively, as shown in figure 2.5.

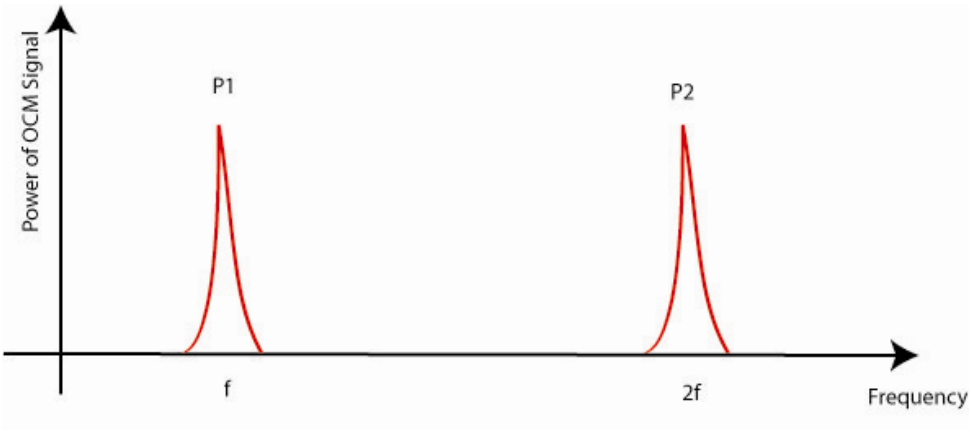

(a)

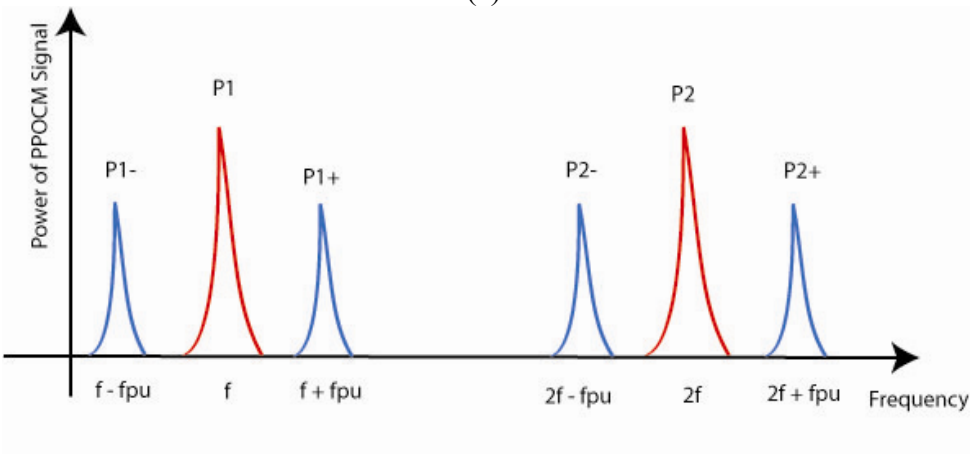

(b)

Figure 2.5 Schematic diagram of the power of OCM signal. (a) and PPOCM signal (b) in Fourier domain. f: fundamental frequency; 2f: second harmonic signal; f_{pu}: the modulation frequency of pump.

2.3 Results and Discussion

The microscope image of tissue sample is shown in figure 2.6 A [35]. We cut a ~1 mm thick section from fixed human skin containing a nodular melanoma. The boundary area between melanotic and amelanotic regions can be observed clearly. We scanned the sample over a field of view of 135 μm by 90 μm (270 by 180 pixels) at a depth of ~26 μm. The pump and probe power on sample were 2.37 mW and 1.29 mW, respectively. The pump beam led the probe beam by 50.5 ps.

The OCM and PPOCM images were acquired simultaneously, as shown in figure 2.6 B and C, respectively. The OCM image shows weak contrast between the melanotic and amelanotic regions. The melanotic region while more highly absorptive than the amelanotic region is also more strongly scattering resulting in a stronger OCM signal in the melanotic region. The PPOCM image shows no signal in the amelanotic region and strong signal in the melanotic region, thus providing good contrast. According to the figure it indicate that melanin is largely on the left side, however, the PPOCM image has some small “islands” of melanin on the right. These islands are not able to see in the OCM image, however they are consistent with the light microscope image in Fig. 2.6 A.

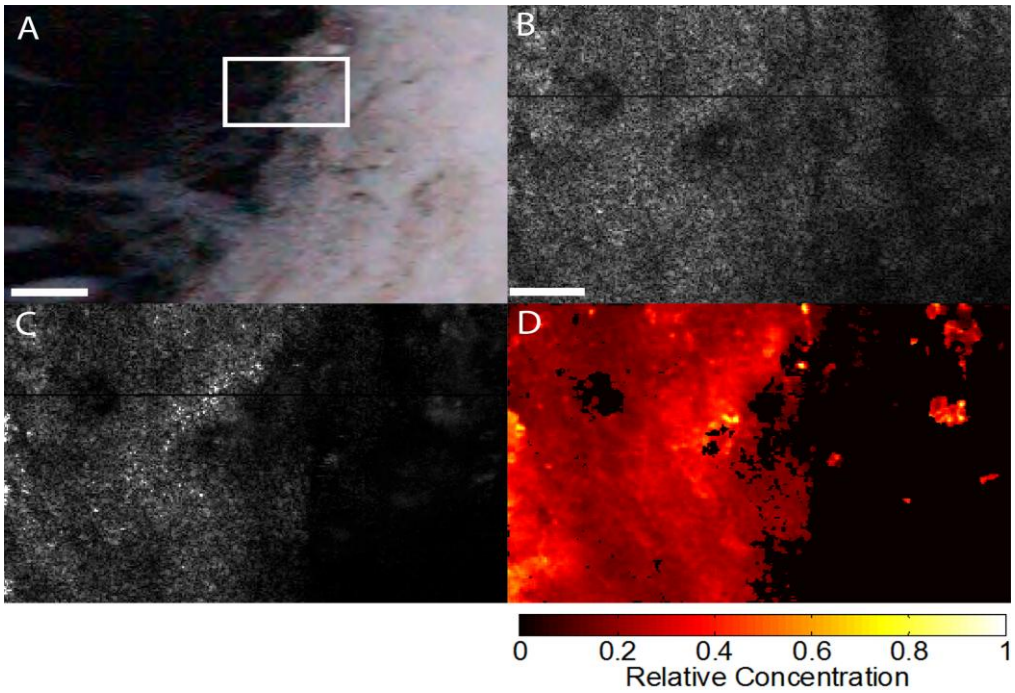

Figure 2.6 Camera image and PPOCM image. A) Light microscope image of the fixed nodular melanoma sample. The scale bar is 100 µm. The box indicates the approximate region where the OCM and PPOCM images were recorded. B) OCM image. The scale bar is 20 µm. C) PPOCM image. D) PPOCM/OCM ratio image depicting the relative melanin concentration. Images B), C), and D) have the same field of view and scale [35].

In addition to just providing molecular contrast, we would like to obtain the relative concentration map of the target chromophore. The PPOCM signal is a function of the chromophore concentration (C), but it is also a function of the tissue reflectivity (R), pump power (P_{pu}), and probe power (P_{pr}). The OCM image is a similar function of P_{pr} and R. At fixed depth, we can make a reasonable assumption which is that the P_{pu} and P_{pr} at that depth is approximately constant over small lateral distances. The ratio PPOCM/OCM, a function of C and P_{pu}, should be a reasonable approximation of the

relative chromophore concentration since P_{pu} is a constant at a given depth in the tissue. This ratio is shown in Figure 2.10 D. We processed the OCM and PPOCM before taking the ratio. We normalized and then spatially averaged over 3 pixels (1.5 μm) in two dimensions to reduce the noise. While the spatial averaging was insufficient to remove the speckle pattern from the OCM and PPOCM images, it is largely absent in the ratio image because the speckle is perfectly correlated. In the regions of the ratio image where there was essentially no PPOCM signal the speckle pattern from the OCM image is apparent. A clear region where the ratio image provides information not available in the PPOCM image is in the largely amelanotic right side of the PPOCM image which in general exhibits very weak signal with a few small islands of modest signal strength. These small islands also correspond to modest OCM signals. In the ratio image, the islands appear as some of the areas of highest melanin concentration. The PPOCM/OCM ratio image not only provides relative chromophore concentration over small lateral distances also cancels the speckle noise to yield a high contrast, low noise molecular image.

2.4 Conclusion

In conclusion, we have developed a novel pump-probe optical coherence microscopy system and imaged melanin in human skin tissue with a nodular melanoma. The results indicate that PPOCM can clearly provide strong contrast between the melanotic and amelanotic regions, which is not available in the scattering based OCM image. We can extend this technique to the early diagnosis of melanoma and the

mapping of tumor margins during excision. We also can extend this application to study other biological chromophore with a known absorption spectrum.

CHAPTER III

SPECTRALLY RESOLVED TWO-COLOR PUMP-PROBE OPTICAL COHERENCE MICROSCOPY

We have discussed that the ground state recovery time and transient absorption spectrum can be used to differentiate among multiple chromophores. In this chapter we present our work of developing a spectrally resolved two-color pump-probe optical coherence microscopy (SRPPOCM) to differentiate two related chromophores.

3.1 Introduction

Previously, we developed a PPOCM which shows good contrast between the melanotic and amelanotic regions, which is not available in the scattering based OCM image. In that study melanin was treated as one chromophore in the melanotic region. However, there are more than one chromophore in melanin, such as eumelanin and pheomelanin. PPOCM is not able to differentiate eumelanin and pheomelanin in a mixture. It is therefore desirable to develop a high-resolution molecular imaging technique which can differentiate multiple chromophores.

Two properties can be used to differentiate among multiple chromophores, ground state recovery time and transient absorption spectrum. Warren and the coworkers have developed a nonlinear microscopy, transient absorption via pump-probe spectroscopy technique [22]. They showed the transient absorption signals of oxyhemoglobin and deoxyhemoglobin [22]. This group has also developed a two-color two-photon and excited-state absorption microscopy system which was used to image

melanin [23]. They mapped out the transient absorption signal by varying the time delay between pump and probe. They also demonstrated that high resolution images could be obtained with different contrasts when various pump and probe pulse delays are considered. This microscopy is based on time resolved pump-probe technique.

We developed a spectrally resolved two-color pump probe optical coherence microscopy (SRPPOCM) technique based on pump-probe spectroscopy and OCM. Absorption spectrum can be mapped out by resolving the spectral dependence of the PPOCM signals at the pump and/or probe wavelengths. It provides specificity for particular chromophores. The specificity may then be used to differentiate between related chromophores like pheomelanin and eumelanin. The ratio of these related chromophores can be an indicator for the diagnosis of early stages of disease, for example, skin cancer.

Currently, melanoma is diagnosed by visually inspecting the skin and by biopsy. Such diagnostic results are subjective among pathologists. This dissertation presents a spectrally resolved pump-probe Optical Coherence Microscopy (SRPPOCM) technique based on pump-probe spectroscopy and Optical Coherence Microscopy (OCM) to facilitate differentiation of the two most common types of melanin found in human skin and hair; pheomelanin and eumelanin. Our preliminary results show that the SRPPOCM technique could provide a strong contrast between pheomelanin and eumelanin. The results also indicate that SRPPOCM could be potentially used as a clinical tool for diagnosing different progression stages of melanoma.

Melanoma is the most common and aggressive type of skin cancer, and the leading cause of death due to skin disease in the United States [37]. According to the American Cancer Society, 68130 melanoma patients were estimated to be diagnosed in 2010 [38].

Current diagnosis process for melanoma involves health care providers visually checking the suspicious skin markings and then requesting a biopsy for further diagnosis. This diagnostic process is subjective and involves variations among pathologists at times yielding false conclusions. In 2010 Shoo and coworkers reported a discordance rate of 14.3 % for melanomas and nevi among pathologists [39]. This translates to an estimated 214,500 to 643,500 cases which would be diagnosed differently [39]. As a consequence of disagreements, normal tissues in the vicinity of suspicious tissues may have also been removed. The superfluous removal of tissue can dramatically change the quality of life of the patients, and increase healthcare costs unnecessarily. Therefore, it is desirable to develop imaging techniques which provide more accurate and objective diagnosis of melanoma.

Melanoma is an uncontrolled growth of melanocytes, cells found in the basal layer of the epidermis, which produce a skin pigment called melanin. There are two chemically different types of melanin pigments; eumelanin and pheomelanin. Different types of melanin aggregate together with different proportions and bonding patterns. Both pheomelanin and eumelanin are found in human skin and hair, and eumelanin is the most common form of biological melanin in humans. Eumelanin is brown to black in color and is metabollized from copolymerization of 5,6-dihydroxyindole (DHI) and 5,6-

dihydroxyindole-2-carboxylic acid (DHICA) [40]. Pheomelanin is metabolized from 5,6-indolequione, and contributes to colors light brown, yellow, and red [41].

Research studies have shown that people with varying melanin would be expected to have different risk factors for developing skin cancer or melanoma [42]. It also has been shown that the amount of pheomelanin found in melanoma is significantly higher than the amount of pheomelanin in normal skin or nonmalignant nevi [43-45]. These results indicate that the ratio of pheomelanin to eumelanin could potentially provide a clinical tool of diagnosing the progressive stages of skin cancer due to melanoma. Thus, it is desirable to develop optical molecular imaging microscopy techniques which could differentiate the pheomelanin from eumelanin or measure the ratio of the two chromophores.

Warren's group has reported a technique based on pump-probe spectroscopy that directly differentiates pheomelanin from eumelanin in pigmented lesions of human skin by varying the delay time between pump and probe [46]. They developed a multiphoton imaging technique via pump-probe spectroscopy that imaged eumelanin and pheomelanin in pigmented lesions of human skin [46]. The imaging system developed by Warren and coworkers is similar to our system with two important differences. Our imaging system works in the epi direction as optical coherence microscopy only works in epi detection. Coherent gate rejects multiple scattered light which can overwhelm the pump-probe signal in a highly scattering medium. Thus, pump-probe images from our system have less background from multiple scattered light and lower noise levels.

3.2 Material and Methods

3.2.1 Optical System

We first developed an inexpensive method to generate two synchronized pump beams at different wavelengths. The optical system is shown schematically in figure 3.1. A tunable source was broadened, as shown in figure 3.2 A, by launching approximately 300 mW of light from a 780nm 140 fs Ti:Sapph laser (80 MHz) into a 2 m length photonic crystal fiber (PCF). The beam was then passed through a dichroic mirror and two bandwidth filters to generate two pump beams at wavelengths 635 nm and 730 nm as shown in Figure 3.2 B. A dual frequency chopper was used to chop the pump beams at two different modulation frequencies; 730 nm at 2.90 kHz and 635 nm at 2.07 kHz. Both pump beams were passed through an optical delay line while the polarization angle was rotated 90 degrees after being combined in another dichroic mirror. The probe beam (780nm) was launched into a Mach-Zehnder type interferometer. Several mirrors were used to adjust the delay line in the probe beam so that the optical path length between two pump beams and the probe beam are matched. In the reference arm, a phase modulator driven at resonance (57.25 kHz) by a sine wave provided a carrier frequency for the interferometric signal. The two pump beams were combined with the probe beam by using a polarized beam splitter before being focused onto the sample using a 1.0 NA water immersion objective, which provided sub ~0.5 μm lateral resolution and a measured ~2 μm axial (confocal gate). The delay between pump and probe was matched by a couple of folding mirrors in the probe beam train and adjusted by the translation stage in the pump beam train. A 2X2 (50/50) single-mode fiber coupler served as the

confocal pinhole which also combined the sample beam and the reference beam in the interferometer. The two outputs of the fiber coupler were connected to a 125 kHz dual balanced detector. En face imaging was accomplished by translating the sample using a high precision translation stage. The measured SNR of the OCM system was 121 dB, 6 dB difference from the shot-noise limit of 127 dB.

We still used the same algorithm [36] to calculate the intereferometric signal (S_{OCM}). The signal is the square root of the sum of the power at phase modulator frequency (P_1) and the 2nd harmonic (P_2), $S_{PPOCM} = \sqrt{P_1 + P_2}$. The sidebands were generated on P_1 and P_2 at +/- the two pump modulation frequencies due to the change induced on probe beam by 635nm pump beam and 730 nm pump beam respectively.

The two PPOCM signals are written as

$$S_{PPOCM} = \sqrt{P_{1-} + P_{2-}} + \sqrt{P_{1+} + P_{2+}}$$

$$S'_{PPOCM} = \sqrt{P_{1'-} + P_{2'-}} + \sqrt{P_{1'+} + P_{2'+}}$$

where + and – subscripts indicate the plus and minus sidebands, respectively. S_{PPOCM} represents the PPOCM signal at 635nm and $S_{PPOCM'}$ represents the PPOCM signal at 730 nm. Figure 3.3 shows the schematic diagram of the power of SRPPOCM signal in Fourier domain.

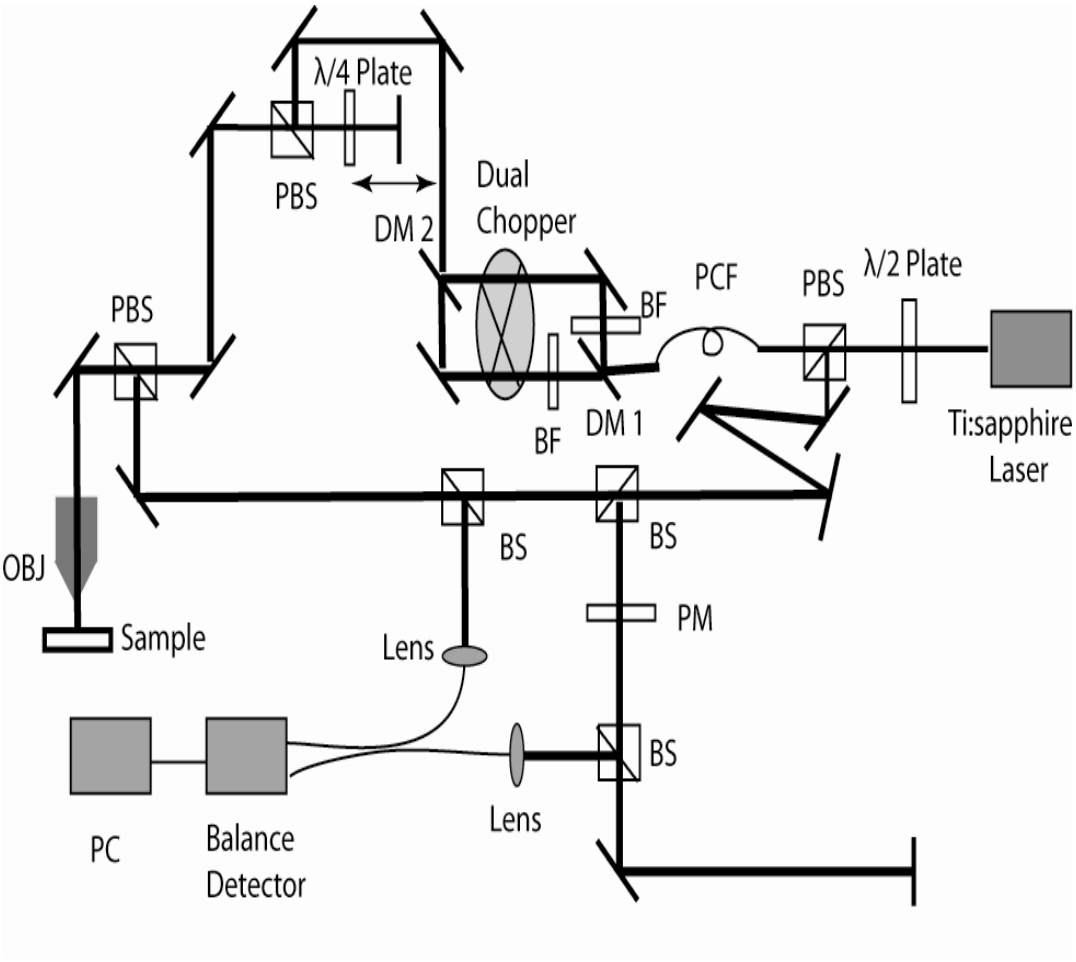

Figure 3.1 Schematic diagram of the SRPPCM. PCF: photonic crystal fiber; Obj: objective; BS, beam splitter; PBS; polarized beam splitter; BF, band pass filter; DM, dichroic mirror, 2X2; 2X2 50:50 fiber coupler; PM: phase modulator.

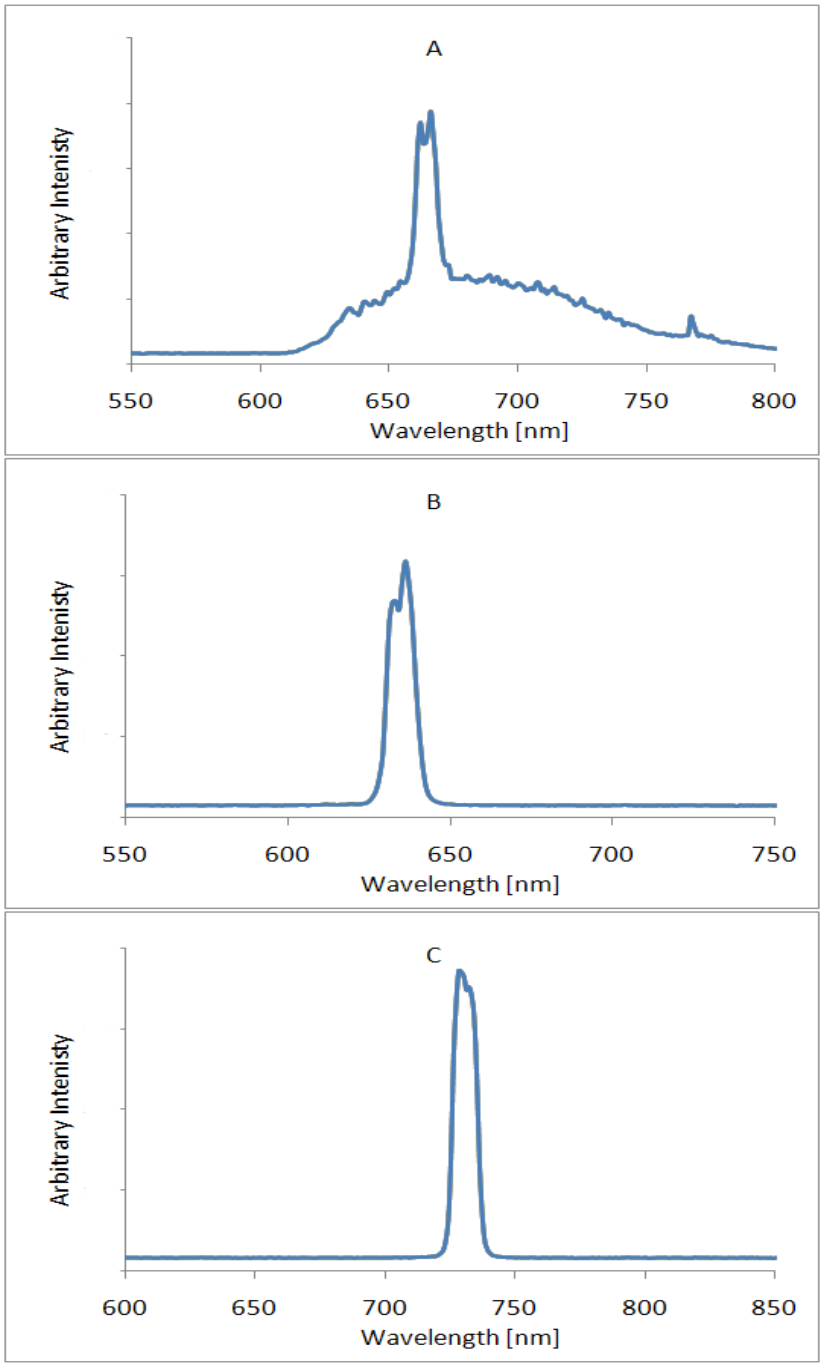

Figure 3.2 Representative source spectrums of SRPPOCM. A) Representative source spectrum after exiting the PCF. B) Representative pump source spectrum at 635nm. C) Representative pump source spectrum at 730 nm.

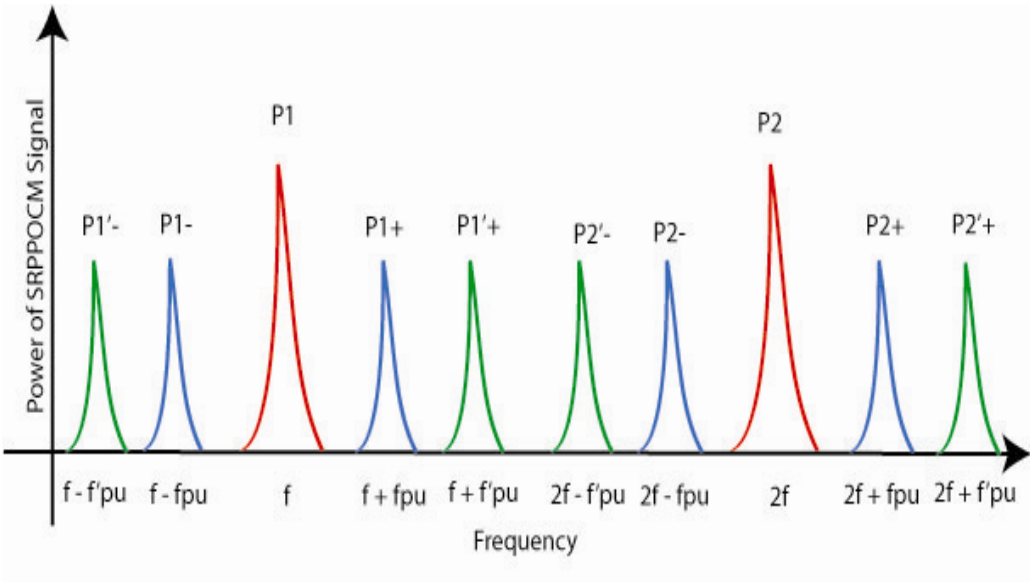

Figure 3.3 Schematic diagram of the power of SRPPOCM signal in Fourier domain. f: fundamental frequency; 2f: second harmonic signal; f_{pu}: the modulation frequency of pump at 635 nm; f'_{pu}: the modulation frequency of pump at 730 nm.

3.2.2 Modeling

If we vary the pump wavelength while fixing the probe wavelength in PPOCM, we can map out the transient absorption spectrum and thus differentiate among multiple chromophores. In this dissertation we generated two pump beams instead of scanning the pump wavelength over a long range with a certain wavelength increment based on two reasons. The first reason is that we wanted to use an inexpensive way to generate two pump beams. Resolving the spectral dependence of the PPOCM signal at the two pump wavelengths will provide the relative concentration map of the two chromophores thus providing contrast between them. In order to be able to differentiate pheomelanin

from eumelanin, we derived a model based on the relationship between PPOCM signals and the concentrations.

The PPOCM signal can be written as the following [32]:

$$S \approx \frac{R\rho\Delta t}{2e}\left(\frac{\sigma_1\sigma_2 z N_1^0 \lambda_{pu} P_{pu}}{hc\pi w_0^2 f_0}\right)^2 P_{pr} \tag{3-1}$$

where R is the sample reflectivity, ρ is the detector responsivity, P_{pr} is the sample arm power in the OCT interferometer, t is the integration time, e is the electron charge, f_0 is the laser pulse repetition rate, $N_1(t)$ and $N_2(t)$ are the time dependent ground and excited state populations integrated over the pump pulse duration, N_1^0 is the ground state population before interacting with the pump laser, σ_1 and σ_2 are the absorption cross section at pump and probe wavelengths, z is the absorption path length, λ_{pu} is the pump wavelength, P_{pu} is the average pump power, ω is the pump modulation frequency, h is Planck's constant, c is the speed of light, and w_0 is the focal spot radius.

Thus, the PPOCM signals at λ_1 and λ_2 can be written as the following for application on pheomelanin and eumelanin, respectively:

$$S^2(\lambda_1) \sim (\sigma^p(\lambda_1)C^p + \sigma^u(\lambda_1)C^u)\lambda_1 P_1 \tag{3-2}$$

$$S^2(\lambda_2) \sim (\sigma^p(\lambda_2)C^p + \sigma^u(\lambda_2)C^u)\lambda_2 P_2 \tag{3-3}$$

And then taking the ratio and rearranging we can have

$$\frac{C_p}{C_t} = \frac{S^2(\lambda_2)a\lambda_1 P_1 - S^2(\lambda_1)bc\lambda_2 P_2}{S^2(\lambda_1)(1-b)c\lambda_2 P_2 + S^2(\lambda_2)(a-1)\lambda_1 P_1} \tag{3-4}$$

where, $S(\lambda_1)$, $S(\lambda_2)$ are PPOCM signal due to the mixed chromophores (pheomelanin and eumelanin) at two different pump wavelength of λ_1 and λ_2. C_p is the concentration due to pheomelanin and C_t is the total concentration due to pheomelanin and eumelanin.

P_1 and P_2 are the power at λ_1 and λ_2. The coefficient of a, b, c are the defined by the following equations:

$$\sigma^u(\lambda_1) = a\sigma^p(\lambda_1)$$

$$\sigma^u(\lambda_2) = b\sigma^p(\lambda_2)$$

$$\sigma^p(\lambda_2) = c\sigma^p(\lambda_1)$$

where $\sigma^u(\lambda_1), \sigma^p(\lambda_1), \sigma^u(\lambda_2)$ and $\sigma^p(\lambda_2)$ are the absorption cross section of eumelanin and pheomelanin at the two pump wavelength λ_1 and λ_2, respectively. These absorption cross section coefficients can be obtained from the paper of Zonios and coworkers [47]. The coefficients a, b and c are 2.2233, 3.071 and 0.5192 respectively.

3.3 Results and Discussion

We chose hair to be our initial sample. The sample is a 20mm stand of red human hair (primarily contain pheomelanin) and a black human hair (primarily contain eumelanin) sitting side by side on a metal washer with 13mm outer diameter as shown in figure 3.4 . The two ends of the strand hair were glued to the washer to avoid them moving during imaging. The sample was scanned with the PPOCM system over a field of view of 18.5 μm by 214 μm at a depth of ~20 μm. The power of the two pump beams at 635nm and at 730nm were 0.61 mW and 0.31 mW, respectively while the probe power was 2.3mW, with the two pump beams leading the probe by 33.3 ps.

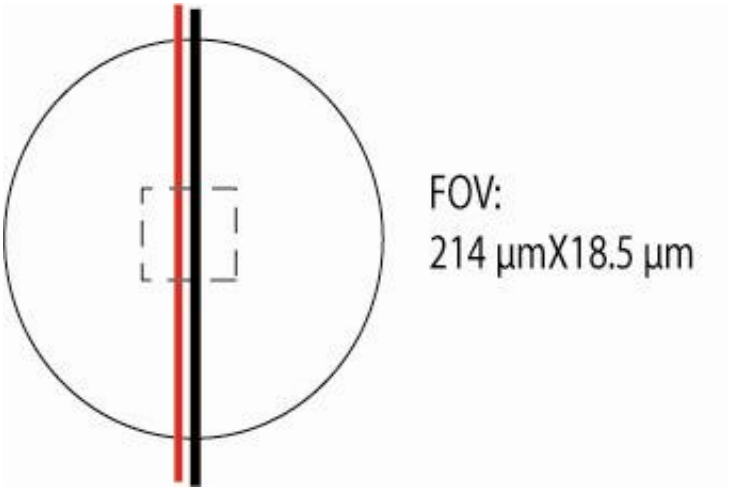

Figure 3.4 A red hair and black are side by side on a metal washer. The square (dashed line) indicates the size the FOV.

The OCM image and two PPOCM images at λ_1 and λ_2 were acquired simultaneously, as shown in Figs 3.4 A, B and C, respectively. The OCM image shows strong OCM signal from black hair (left side) and red hair (right side) due to scattering, however, there is no contrast between black hair and red hair. The two PPOCM images (at 635nm and 730 nm) show poor contrast between black hair and red hair, which indicate that left side hair has stronger PPOCM signal than right side hair. This result is consistent in both PPOCM images. However, we can't differentiate the two color of hair if we don't know which side is black hair and which side is red hair at the first place. In addition, we can't obtain the information of relative concentration of pheomelanin to the total melanin either from the two PPOCM images. In order to be able to differentiate pheomelanin from eumelanin, we applied the model we derived and obtained the figure 3.5 D. This is the relative concentation map of pheomelanin to total melanin (eumelanin and pheomelanin). As shown in figure 3.5 D, the ratio PPOCM image indeed indicates

that black hair is on left side and red hair is on right side. According to the figure 3.5 D, as we expected, eumelanin is the dominated melanin in black hair and pheomelanin is the dominated melanin in red hair. Before taking the ratio both PPOCM images were spatially averaged over 5 pixels (2.5 μm) in both dimensions to reduce the noise. The SNR of PPOCM signals were further thresholded at 5. The relative concentration image provides relative pheomelanin concentration map and shows strong contrast between pheomelanin and eumelanin.

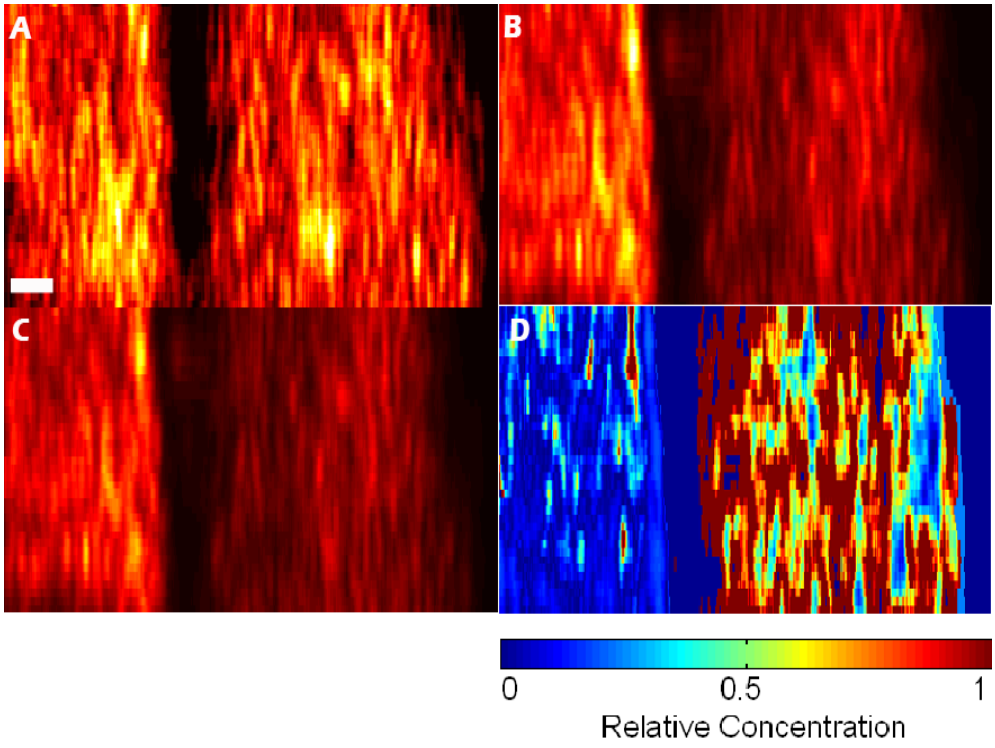

Figure 3.5 OCM, PPOCM images and relative concentration images. A) OCM image. The scale bar is 20 μm. B) PPOCM image at 635nm. C) PPOCM image at 730nm. D) Relative concentration of pheomelanin. Images A), B), C), and D) have the same field of view and scale.

This is our first step to differentiate two related chromophores in a mixture by using SRPPOCM. We can obtain a, b and c by using a pure pheomelanin and eumelanin sample on this SRPPOCM system which is more precise method to validate the model we derived.

3.4 Conclusion

We first developed an inexpensive method to generate two pump beams at different wavelengths. We can obtain an OCM image and two PPOCM images at two different pump wavelengths simultaneously through SRPPOCM. By applying a model we derived, we can obtain a relative concentration map of pheomelanin. We tested this system on a red-black hair sample, and the results indicate that SRPPOCM can provide strong contrast between pheomelanin and eumelanin. This result is not available either in the scattering based OCM image or in one color pump-probe optical coherence microscopy. SRPPOCM can be used to obtain the ratio of pheomelanin to eumelanin to further characterize important physiological parameters of tumors and can be potentially used as a clinical tool for diagnosing different progression stages of melanoma. This technique can also be extended to differentiate other related chromophores.

CHAPTER IV

SECOND HARMONIC OPTICAL COHERENCE TOMOGRAPHY TAGGING NANOCRYSTAL

In this chapter, we will present our preliminary study of feasibility of collecting backward SHG signal to address the depth ambiguity issue in SHOCT.

4.1 Introduction

4.1.1 Disadvantages of Optical Coherence Tomography

OCT is a well known noninvasive optical imaging modality. OCT measures the internal microstructure of biological samples by measuring backreflected and backscattered light. Same as OCM system, it uses coherence gating of backscattered light to obtain images. The first clinical application was in ophthalmology for the imaging and diagnosis of retinal diseases [48]. It provides cross-sectional tomographic images with micrometer scale resolution [49].

Despite many advantages of OCT, poor contrast is the major limitation. This is because the contrast in OCT images depends upon the inhomogeneities of sample scattering properties, which is linearly dependent on different local refractive indices of a sample. In many cases, the changes of linear scattering properties in sample are relatively small and difficult to measure. Confocal fluorescence microscopy, two-photon microscopy and second-harmonic microscopy have been developed to enhance the capability to measure molecule specific signals. However, OCT can't take the advantage

of using fluorescence modality due to its coherent detection method. Only the molecular processes that result in coherent emission of light can be applied to OCT. These coherent processes include pump–probe OCT, CARS, and SHG.

4.1.2 Second Harmonic Optical Coherence Tomography

SHG is a coherent process and shows a nonlinear relationship between polarizability and the applied electric field exists. The process generates light with precisely twice the fundamental frequency.

If we use induced polarization to describe the optical response of a linear sample, the relationship between the polarization and electric field can be expressed as:

$$P = \varepsilon_0 \chi^{(1)} E \tag{4-1}$$

where $\chi^{(1)}$ is the linear susceptibility.

For nonlinear optics the induced polarization can be expended by Taylor expansion and thus we have [50]:

$$P_k = \varepsilon_0(\chi_{ik}^{(1)} E_i + \chi_{ik}^{(2)} E_i E_j + \chi_{ik}^{(3)} E_i E_j E_l + \cdots) \tag{4-2}$$

where the coefficient $\chi^{(n)}$ is the tensor of the nth order nonlinear process.

The electric field is

$$E_i = \varepsilon_i \exp(-i\omega t) \tag{4-3}$$

where ε_i is the amplitude. If we only consider the second order term and plug the electric field into equation (4-2) we will have [50]:

$$P_2 = \chi_{ijk}^{(2)}(\varepsilon_i \varepsilon_j \exp(-i2\omega t) + \varepsilon_i^* \varepsilon_j^* \exp(-i2\omega t) + \varepsilon_i \varepsilon_j^* + \varepsilon_i^* \varepsilon_j) \tag{4-4}$$

It is obvious that the second order polarization contains a component at 2ω and a DC component. We will ignore the DC term and only consider the second harmonic term. If the material has inversion symmetry the even-order coefficients disappear because these coefficients are cancelled out due to the minus signs. This only happens for even-order coefficients. Most materials have inversion symmetry and thus the second harmonic signals can only be obtained in a non-centrosymmetric medium. The strength of SHG signal can be enhanced by increasing average intensity or peak intensity of laser pulses.

The incident beam with random phases generates the dipoles inside the non-centrosymmetric material that radiate weak SHG signal as their phase is random. However, if relative phase of the incident beam is fixed inside the non-centrosymmetric material, the induced dipoles radiate at 2ω with a fixed relative phase. Due to phase matching, the contribution can be added up constructively at the end of the material. This is referred to as phase-matching which is important to obtain a second harmonic signal.

We can also show this process in an energy diagram (figure 4.1). In SHG, a molecule is excited from the ground state to a virtual excited state. When the molecule returns from the virtual excited state to the ground state, it emits a photon with second harmonic frequency. The power of the second harmonic is proportional to the square of the power in the fundamental.

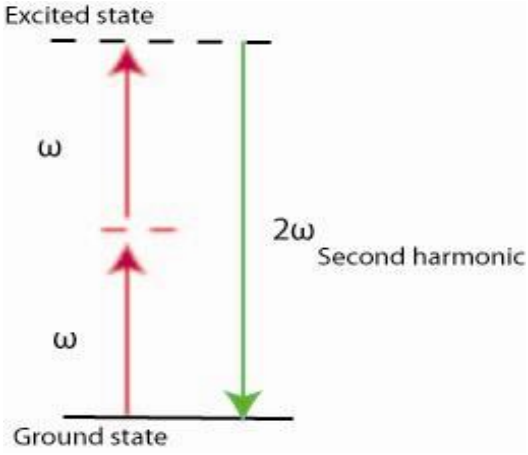

Figure 4.1 Energy diagram of SHG

SHG shows strong contrast in nonlinear optical microscopy. SHG microscopy provides high resolution images since the signal is only collected in the focal volume of the objective with high numeric aperture. In general it is difficult to obtain transmission SHG images in thick tissue. SHG microscopy that collects backscattered light has been reported [51]. SHG can occur only in a non-centrosymmetric medium in the electric dipole approximation. SHG signal can be observed in cell membranes and highly ordered structures, such as collagen fibers and microtubule ensembles [52, 53, 54]. SHG provides a powerful tool for nonlinear optical imaging modality in biomedical and biological research.

4.1.3 Fourier-Domain Second Harmonic Optical Coherence Tomography

As we disused earlier, SHG, being a coherent process, can be adapted to OCT to image non-centrosymmetric biological samples. Similar to the general OCT, SHOCT has two types, time-domain SHOCT (TD-SHOCT) and Fourier-domain SHOCT (FD-SHOCT). Researchers found that Fourier-domain SHOCT is also more sensitive than

time-domain SHOCT [55, 56, 57]. In this dissertation, we will emphasis on Fourier-domain SHOCT.

4.1.4 Advantages and Depth Ambiguity of SHOCT

SHG does not bleach over time and the generated signal is stable. In addition, unlike fluorescence based techniques, the choice of excitation wavelength is flexible. SHG provides a strong and a unique image contrast mechanism in tissue structure and local symmetry changes for non-centrosymmetric biological samples. A three-dimensional sectioning of the sample can be obtained if a high numeric aperture objective is used in the sample arm. However, in a high scattering sample, the resolution and imaging depth decreases due to scattering light from the non-focal regions. By combining SHG and OCT, the resolution can be improved as the coherence gate rejects the backreflected light from regions out of focus. For a SHOCT, one can obtain general OCT image and SHG image simultaneously.

However, depth ambiguity exists in SHOCT. Considering the second harmonic signal generated in a bulk non-centrosymmetric crystal at a certain depth in the tissue, if the second harmonic photons are immediately backscattered, the detected SHG signal will correctly report the depth at which the signal is generated. However, if the SHG light still keeps propagating deeper into the tissue before being backscattered, the measured forward generated second harmonic will not report the correct depth due to the further propagating. Currently no algorithm is available to correct for the depth

ambiguity issue. In addition there could be ~ 40 dB attenuation due to the poor reflectivity of the tissue. This process is illustrated in figure 4.2.

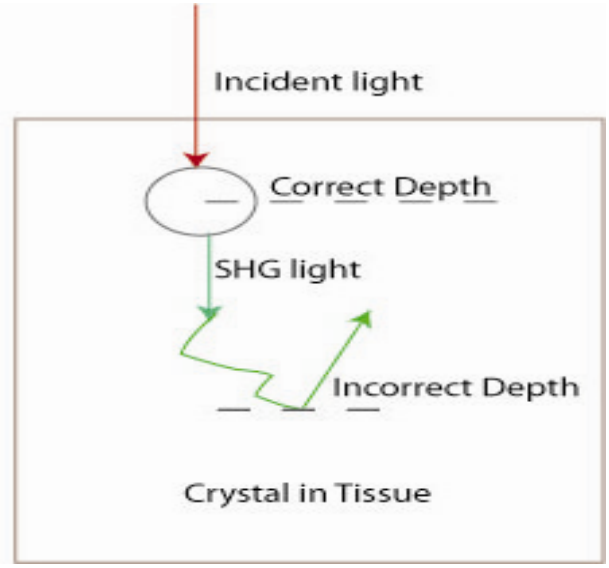

Figure 4.2 Depth ambiguity of SHG crystal in tissue due to the collection of forward generated second harmonic signal. The circle represents the bulk non-centrosymmetric crystal. The red light represents the incident light while the green light represents the second harmonic generated light.

To address this issue we proposed a new SHG molecular contrast mechanism which employs non-centrosymmetric nanocrystals as the SHG contrast agent. Forward and backward generated second harmonic signals are equivalent probability in non-centrosymmetric nanocrystal. However, the forward generated second harmonic signal is reduced by ~ 40 dB due to the poor reflectivity of the tissue. In contrast, the backward generated signal will dominate the forward generated signal. Thus, if we could collect the backward generated second harmonic signal instead of the forward generated one from nanocrystals, the depth will be correctly reported solving depth ambiguity.

4.1.5 Nanoscale Second Harmonic Generation

Molecular symmetry of the sample determines whether second harmonic signal can be generated from a given material, while phase matching condition governs the efficiency of SHG output. In bulk crystals, SHG is a narrow band process as it requires the phase matching condition. The phase matching condition ensures that the SHG light interferes constructively in the forward propagating direction.

The scattering direction of the second harmonic is determined by the size of the scatters. There are two types scattering, Rayleigh scattering and Mie scattering. Rayleigh scattering occurs when the size of the scatter is much smaller than the wavelength of the incident light. Mie scattering occurs when the size of the scatter is much larger than the wavelength of incident light. Forward and backward generated second harmonic signals have equivalent probability in Rayleigh scattering whereas forward generated second harmonic signal has greater probability than backward generated second harmonic signal in Mie scattering, as show in figure 4.3.

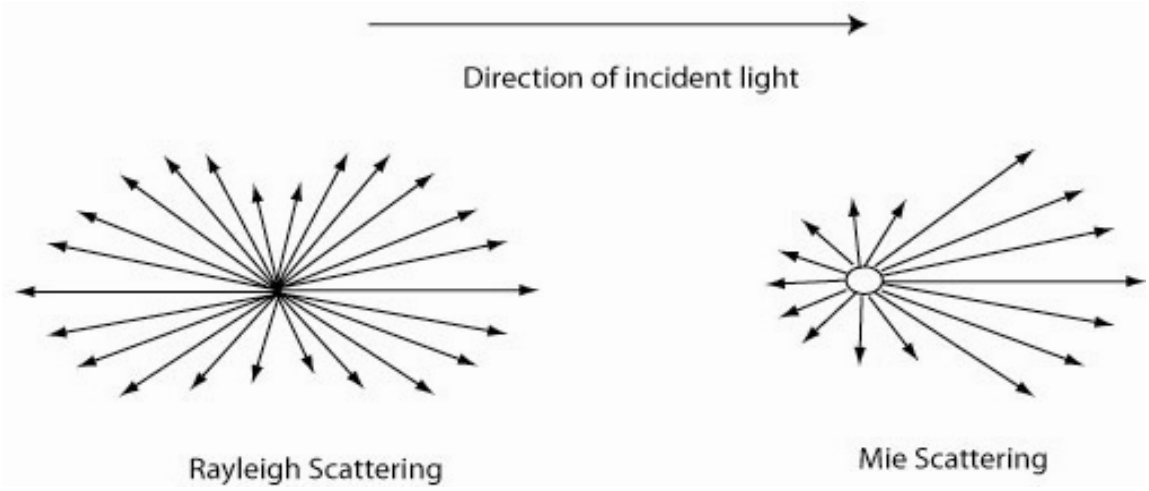

Figure 4.3 Rayleigh and Mie scattering occur for different particles size. When particle size is much smaller than the wavelength of the incident light forward and backward generated second harmonic signals have equivalent probability (Rayleigh scattering). When particle size is much larger than the wavelength of incident light forward generated second harmonic signal has greater probability than backward generated second harmonic signal (Mie Scattering).

We can briefly explain this process based on a non-centrosymmetric nanocrystal SHG material in the experiment. The nanocrystal, barium titanate, is excited by a strong electromagnetic field (E) at fundamental frequency (ω). The internal polarization of the nanocrystal is nonlinear to the external field. Because the nanocrystal is non-centrosymmetric structure it generates a polarization in second harmonic frequency (2ω). Since the physical size of the nanocrystal (~50 nm) is much smaller than the incident wavelength (800 nm), there is no phase matching. Thus, the nanocrystal can be treated as dipole, and the SHG emission will be in all directions. Figure 4.4 shows the direction of the process of SHG in nanocrystal. If the nanocrystals are tagged with biomoeules in a tissue we could collect the backward generated second harmonic light instead of the

forward direction to suppress the depth ambiguity while possibly increasing the sensitivity as shown in figure 4.5.

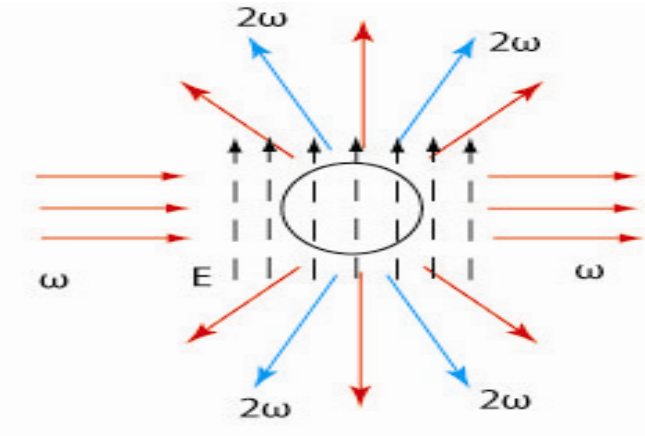

Figure 4.4 Scattering in second harmonic frequency for a non-centrosymmetric nanocrystal structure. Nanocrystal is excited by a strong external field E at fundamental frequency ω.

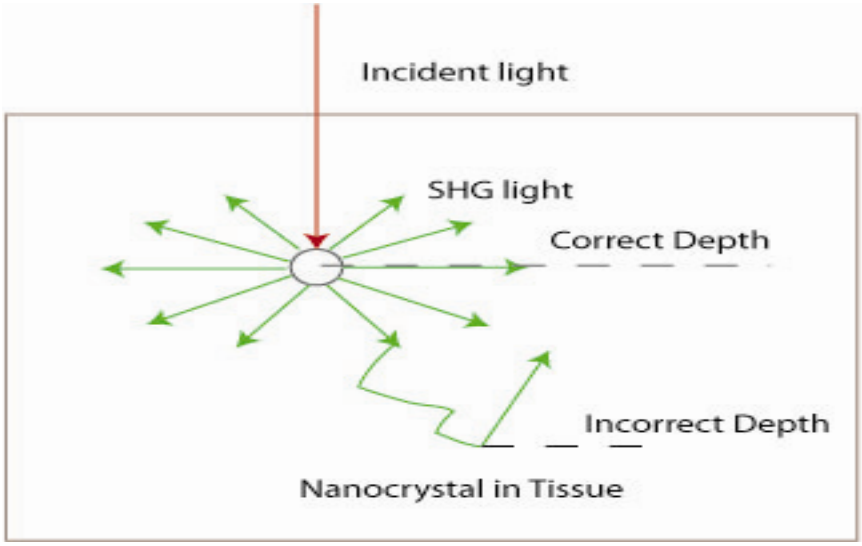

Figure 4.5 To suppress depth ambiguity by collecting backward generated second harmonic signal. The circle represents the nanocrystal. The red light represents the incident light while the green light represents the second harmonic generated light.

4.2 Material and Methods

The setup is based on two Fourier domain OCT systems at IR wavelength (800nm) and SHG wavelength (400nm), respectively. A SHG (400 nm) beam was generated by 50 mW of IR light from a tunable (680-1080 nm) 140 fs Ti:Sapph laser (80 MHz) passing through a second harmonic generator. The light source was pulse-picked before passing through second harmonic generator. The SHG beam was then delivered to a beam splitter and a mirror mounted on a translation stage to form reference arm. The IR reference arm beam passed through a beamsplitter and a dichroic mirror and reflected back from a mirror mounted on another translation stage. After passing through a beamsplitter, the IR beam was then focused onto the sample using a 0.1 NA objective, which offers 678 μm depth of focus. Both reference beam and sample beam at 400 nm were combined in the beamsplitter. The reference beam and sample beam at 800 nm were also combined in the same beamsplitter. After splitting by another dichroic mirror, both 400 nm and 800 nm were then focused on the two separate lenses and delivered to their spectrometers, respectively. The coherence length of the SHG light source is 70 μm. The Schematic diagram of the SHG is shown in figure 4.6.

We chose barium titanate ($BaTiO_3$) as the nanocrystal sample. Before making a nanocrystal slab sample, the nanoparticles were prepared in methanol and spin coated on to a cover slip in order to make a uniform thin film. The first step was to dissolve PVA powder in de-ionized water while heating at ~ 90 degrees Celsius, using a magnetic stirrer until a viscous transparent solution was achieved. We added 0.3 g of BaTiO3 into

14 ml PVA matrix and then placed a drop of BaTiO3 and PVA mixture on the cover slip after cleaning the glass slide with water and then with methanol.

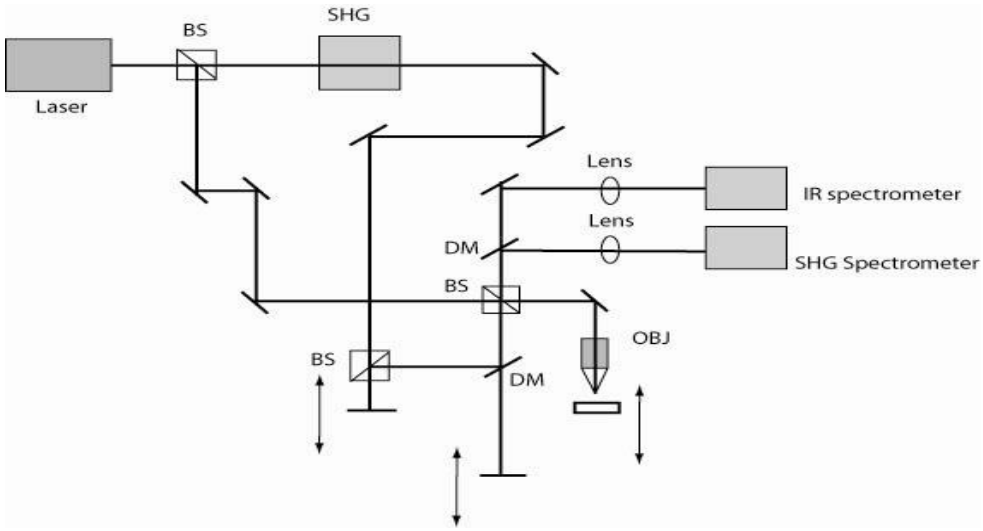

Figure 4.6 Schematic diagram of the two-color SHG. OBJ objective; BS, beam splitter; BS; beam splitter; DM, dichroic mirror; SHG, second harmonic generator.

This process was performed in NanoBio System Labortatory. The nanocrystal slab is shown in figure 4.7. We applied index matching gel between the cover slip and microscope slide. The index matching gel is used to match the refractive indices between spin coated nanocrystal and microscope slide.

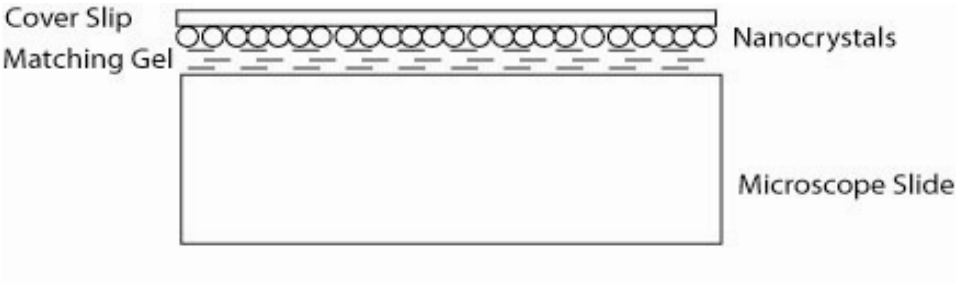

Figure 4.7 Schematic diagram of nanocrystal slab sample. Nanocrystals were sandwiched between a cover slip and a 1mm microscope slide, while index matching gel filled between cover slip and microscope slide.

Before performing this SHG experiment, we characterized the nanocrystal power composition by using X-ray diffraction techniques (XRD). This experiment was done in Naonomaterials and Biophotonics Lab. As shown in figure 4.8, the peaks of the nanocrystal sample match the peaks on the standard data for BaTiO3 XRD figure. So, we confirm that the sample we used is pure BaTiO3 nanocrystal. We know the structure of the BaTiO3 powder is tetragonal shape, non-centrosymmetric material.

4.3 Signal Processing

The Fourier domain OCT usually uses a grating based spectrometer, which disperses the light evenly with respect to wavelength, to separate the spectral contents of the signal. To obtain A-line profile, we need to perform an inverse Fourier transform from k domain (wavenumber) to z domain (depth profile). The intensity value recorded by the spectrometer is evenly spaced at wavelength. The inverse relationship is $k = 2\pi/\lambda$ between wavenumber and wavelength. After transforming, we need to apply a linear interpolation to resample it into points at evenly spaced wavenumber. Then, we performed an inverse Fourier transform analysis to obtain A-line profile. A program flowchart of the signal process is shown in figure 4.9.

The interference spectrums were recorded by the spectrometer and were subtracted by the reference spectrum obtained when blocking the sample arm. All the A-line profiles were averaged over 100 measurements for each position.

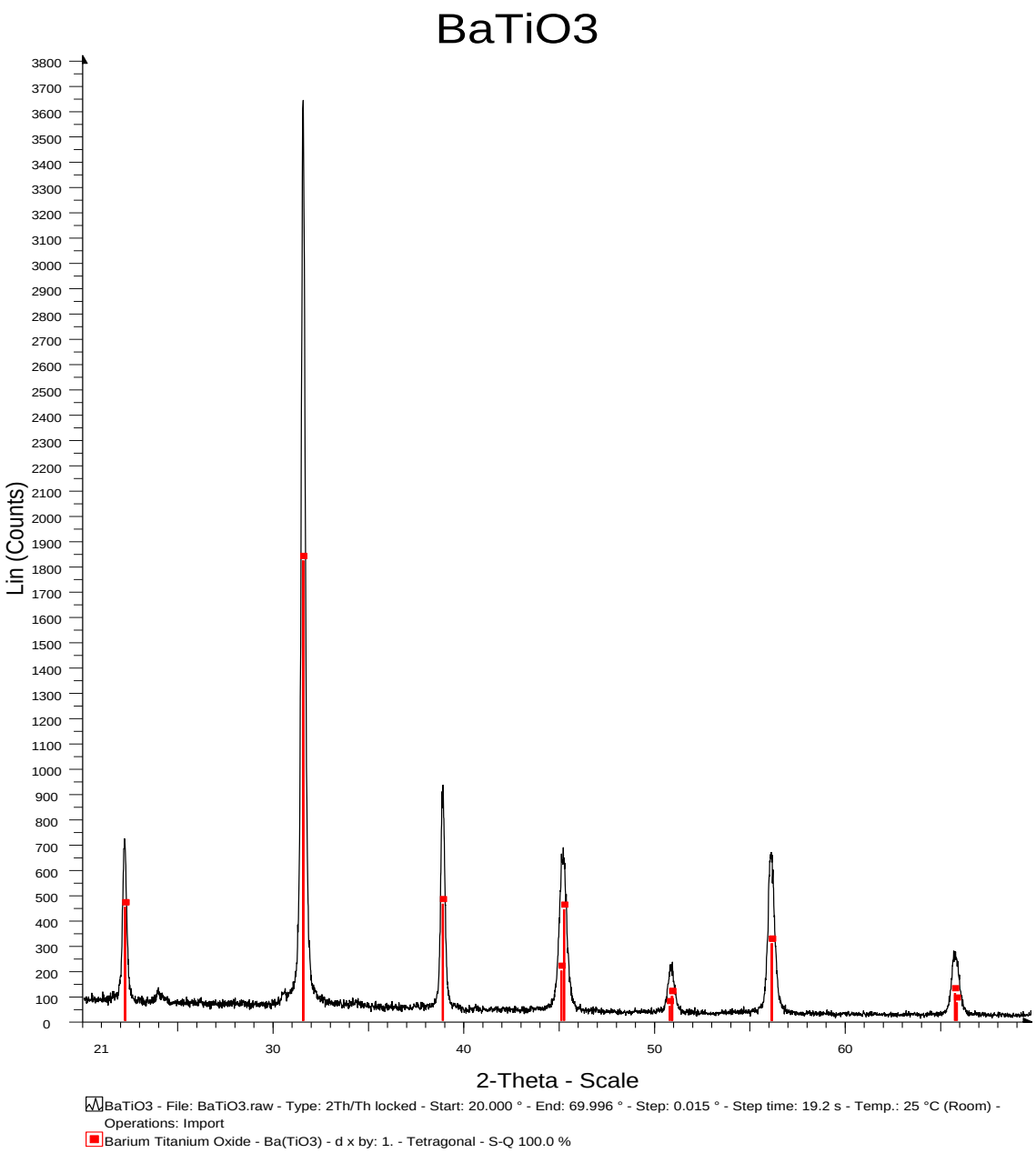

Figure 4.8 Peaks form sample match standard data for BaTiO3, experimental data is in black and standard data is in red.

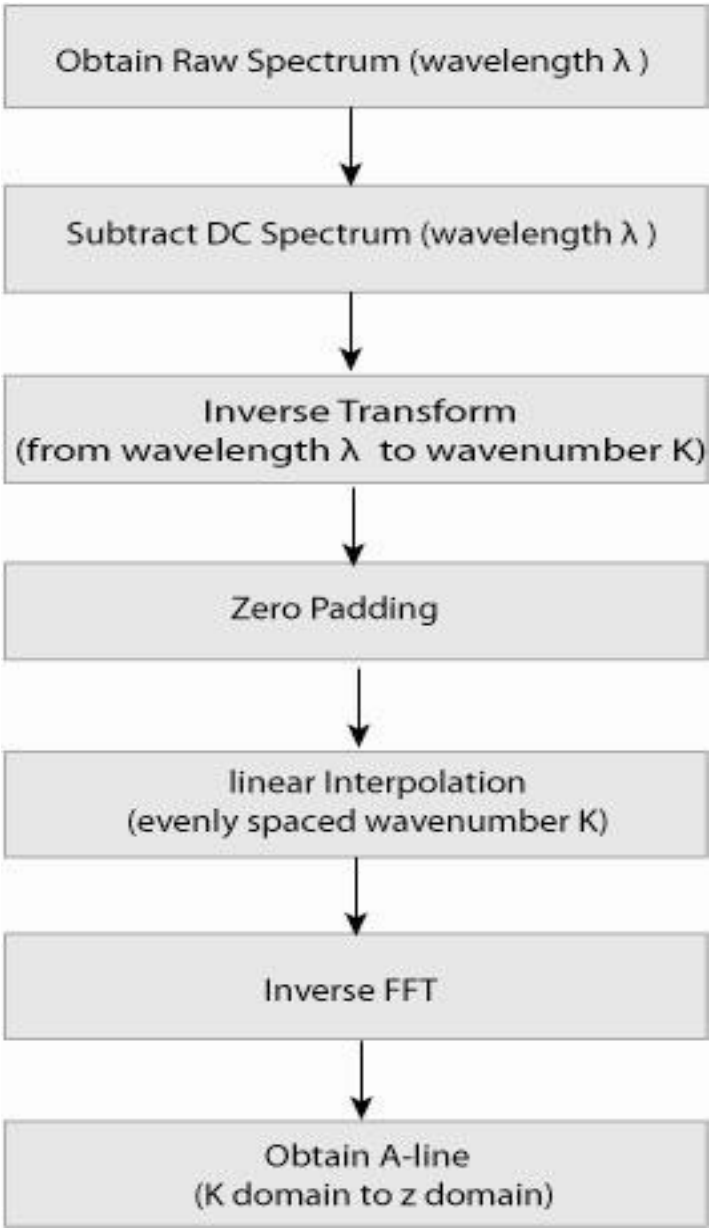

Figure 4.9 A program flowchart of the signal process. It shows how to obtain A-line profile from raw spectrum.

4.4 Results and Discussion

We first performed this experiment to locate the position of the focal plane for the sample arm. A thin layer of nanocrystal powder was deposited on the surface of an aluminum mirror which offers the maximum reflectivity. We moved the sample to the focal plane and adjusted the mirror on the reference arm until we saw the optimized interference fringes through SHG spectrometer and IR spectrometer, respectively. We then set the A-line peak at 100 μm by translating the reference mirrors for SHG and IR wavelength, respectively. Figure 4.10 (a) shows the A-line peak at 100 μm for 400nm of wavelength while figure 4.10 (b) shows that for 800 nm. This experiment is used to provide the baseline of the A-line peaks distance for later measurements.

One thing we need to mention is that the two spectrometers we used only offer 200 μm fall-off which is quite short for FD-OCT system. Fall-off is the reduction in fringe visibility as a function of pathlength difference. It is a function of both the signal averaging over the detectors and the spectral bandwidth of the light interfering at the detector. In FD-OCT, fall-off describes how fast the A-line signal drops as the pathlength difference is increased. Therefore, while moving the objective in the sample arm, we will see that the A-line peaks of 400 nm and 800 nm will move to opposite direction. In other words, if the A-line peak of SHG move toward to DC (zero frequency), the A-line peaks of 800 nm will move away from DC. We can roughly locate the focal plane of the objective for the nanocrystal sample by fixing the position of the reference mirrors at 100 μm for SHG and IR wavelength, respectively.

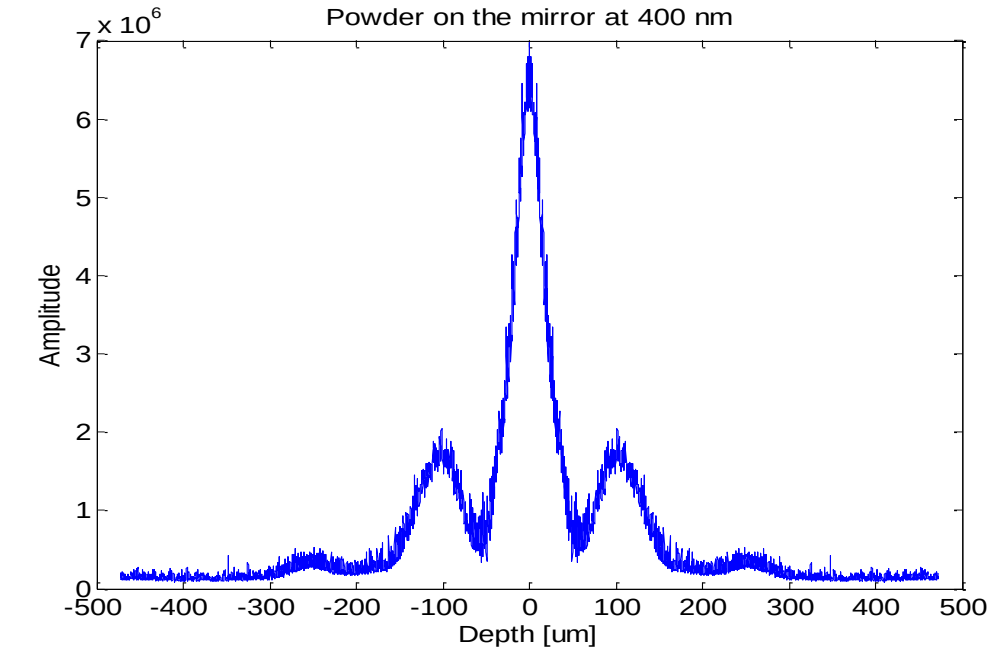

(a)

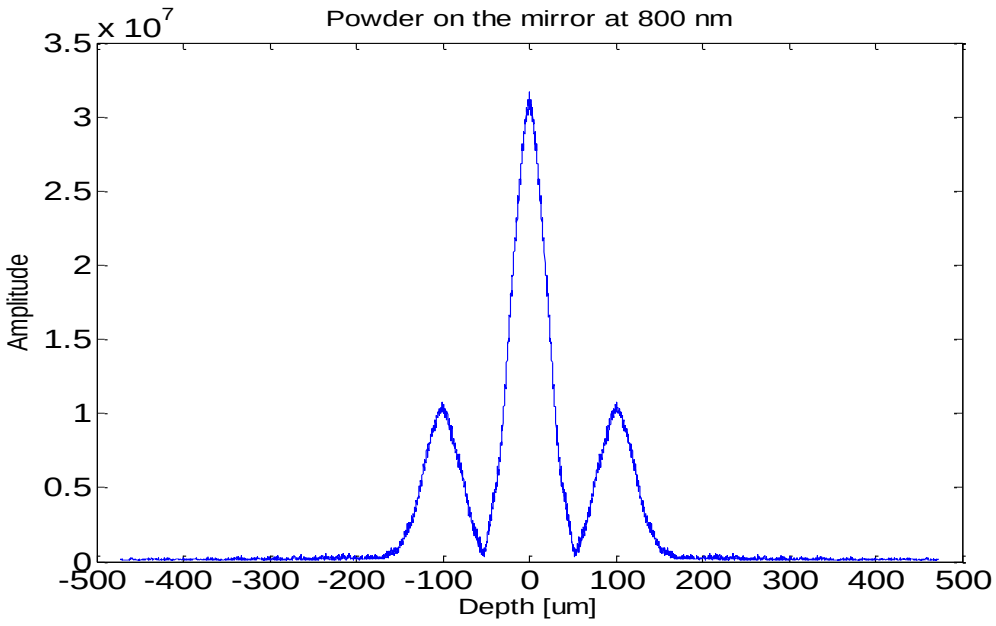

(b)

Figure 4.10 The A-line profile for the sample of nanocrystals deposited on the mirror. (a) at 400 nm. (b) at 800 nm.

We replaced the powder-mirror sample with the nanocrystal slab sample, as shown in figure 4.7. As we described in previous section, we applied refraction index matching gel to match the refraction differences between glass slide, PVA matrix and cover slip so that no reflection occurred from these interfaces. We first moved the sample far away from the focal plane, and then slowly moved the sample closer to the objective. This confirmed that the first A-line peak comes from interference between the first layer of the cover slip and reference mirror fixed at the original position. We optimized the SHG signal by slightly translating the sample in three dimensions. We did not expect to observe the interference signal between the reference mirror and the bottom layer of microscope at 800 nm because the depth of focus of 678 was not long enough to cover the bottom layer of the microscope slide (thickness was 1mm) when the focal plane was at the top layer of the cover slip. In addition, since the index matching gel was used between cover slip and microscope glass slide, there was no interface between them. Accordingly, we can only observe the interference between reference mirror and top layer of cover slip for 800 nm. For the same reason, we did expect that only backward generated second harmonic signal can be measured from the nanocrystal layer as the forward generated second harmonic signal could not be detected. Figure 4.11 shows a schematic illustration of the signals origination for 400 nm and 800 nm.

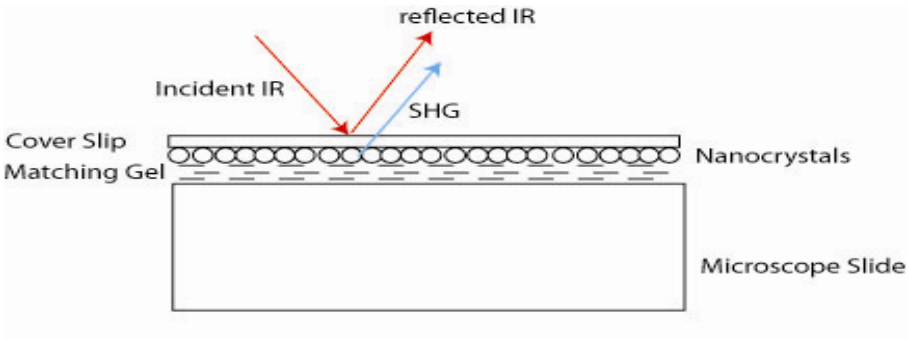

Figure 4.11 Schematic illustration of signal distribution. IR light is in orange and blue light is in blue.

The measured thickness of the cover slip was 170 μm which matched the fact sheet of cover slip. Taking into account the refractive index of glass (1.5), we expected the distance between 400 nm and 800 nm to be 250 μm. The A-line peaks were recorded at three different positions of the nanocrystal sample as shown in figure 4.12, figure 4.13 and figure 4.14, respectively.

In figure 4.12, the A-line peak is at 98 um and 153 um, at 400 nm and 800 nm, respectively. In figure 4.13, the A-line peak is at 72 μm and 182 μm, at 400 nm and 800 nm, respectively. In figure 4.14, the A-line peak is at 85 μm and 165 μm, at 400 nm and 800 nm, respectively. Note that the position of SHG signal and IR signal crosses DC due to the poor fall off of the spectrometer. In other words, to obtain the distance between the two A-line peaks, we needed to take the summation of the peak position instead of the difference. The result can be summarized in Table 4.1.

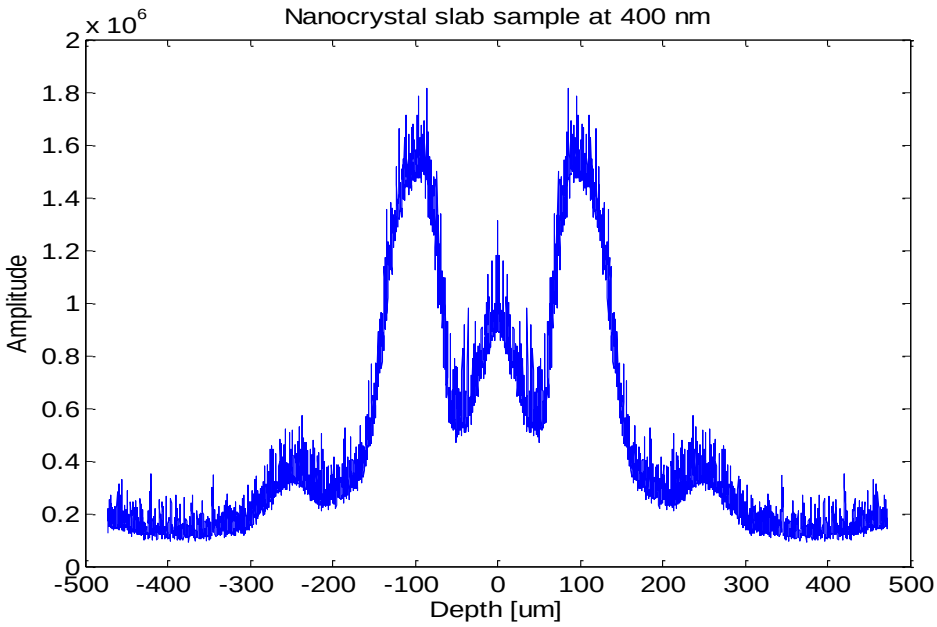

(a)

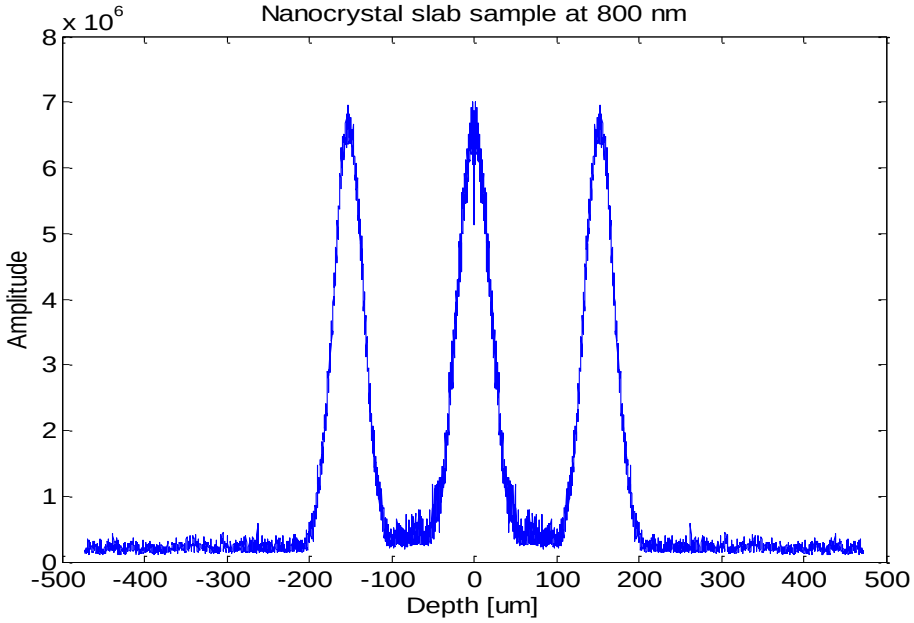

(b)

Figure 4.12 The 1st set of A-line profile for the nanocrystals slab sample. (a) at 400 nm. (b) at 800 nm.

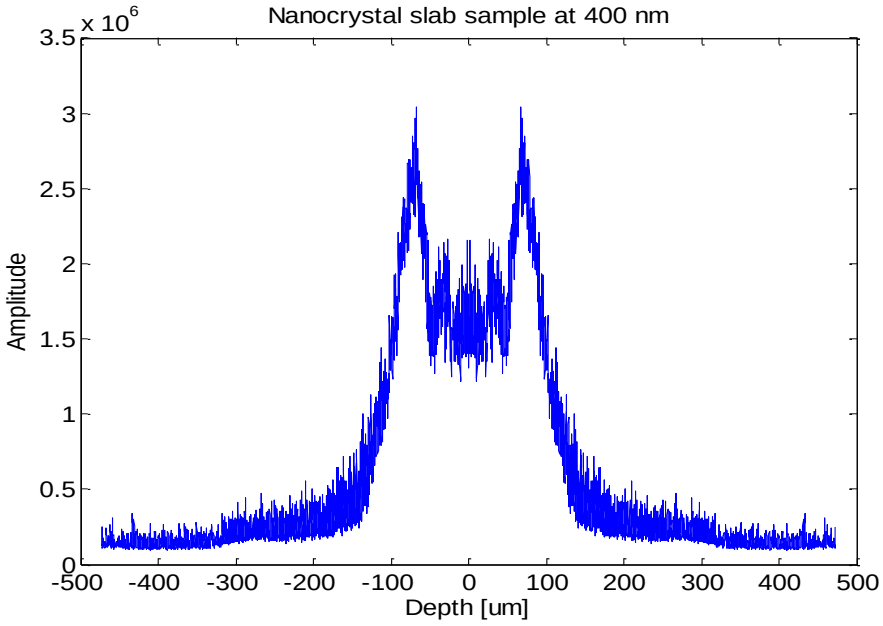

(a)

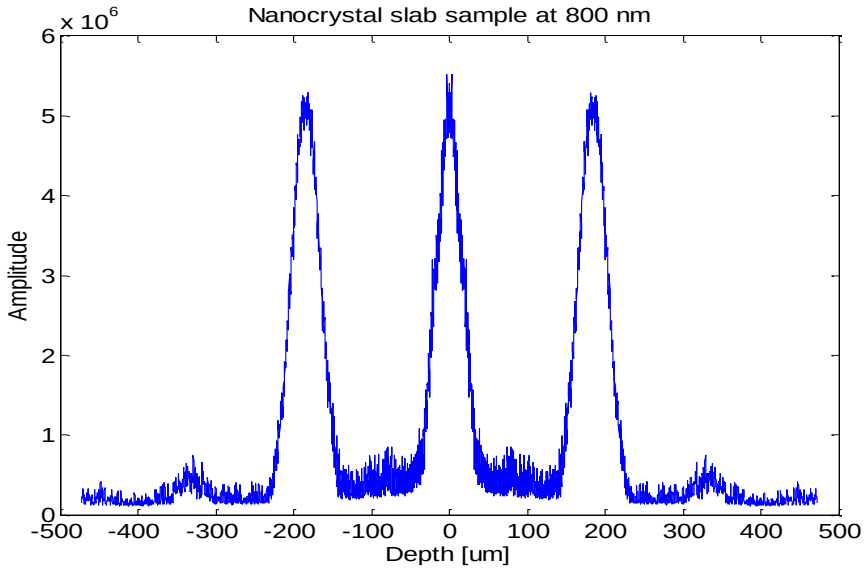

(b)

Figure 4.13 The 2nd set of A-line profile for the nanocrystals slab sample. (a) at 400 nm. (b) at 800 nm.

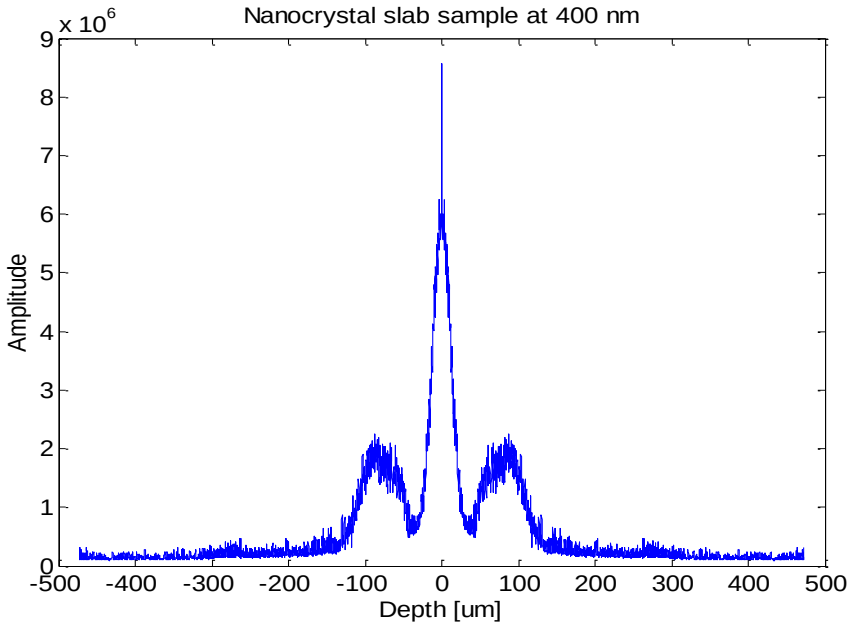

(a)

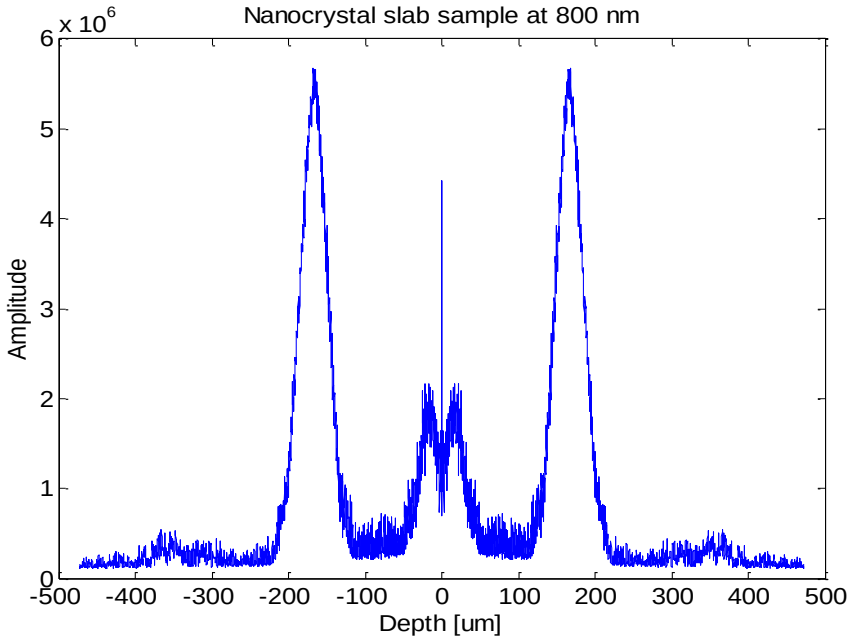

(b)

Figure 4.14 The 3rd set of A-line profile for the nanocrystals slab sample. (a) at 400 nm. (b) at 800 nm (b).

Table 4.1 Summary of the distance of A-lines of 400 nm and 800 nm

	A-line peak at 400 nm [μm]	A-line peak at 800 nm [μm]	Distance [μm]
Position 1	98	153	251
Position 2	72	182	253
Position 3	85	165	250

As shown in Table 4.1, the distance between the two peaks is around 250 μm to 253 μm, which is very close to the optical thickness of the cover slip, 255 μm, as we measured. The result indicates that the interference of 800 nm was generated between the reference mirror and the top layer of the cover slip whereas the interference of 400 nm was created between the reference mirror and the nanocrystal layer. This confirms that the measured SHG signal came from the backward generated second harmonic signal. We could potentially apply this technique to eliminate the depth ambiguity in SHG and to provide better molecular contrast for biological sample since this depth information is correctly reported. Using SHG from non-centrosymmetric nanocrystals as a new type of marker, it can offer stable, non-saturating and coherent signal with ultrafast response time. It also provides a broad choice of excitation wavelength without photobleaching. The nanocrystals can be processed for specific labeling in biomedical applications to improve molecular contrast, whereas the current molecular imaging techniques cannot provide these important functionalities.

4.6 Conclusion

In general, depth ambiguity associated with SHG is not clearly reported by collecting the forward generated second harmonic signal in the tissue. We performed a preliminary study to validate the feasibility of the collection of the backward generated second harmonic signal from non-centrosymmetric nanocrystals, $BaTiO_3$, via a Fourier domain SHOCT system. Based on this study, we could apply this technique to collect backward generated second harmonic signal from the tissue sample which reports the correct depth of SHG origination, and suppress the depth ambiguity in SHOCT. The nanocrystals can be processed for specific labeling in biomedical applications to improve molecular contrast, whereas the current molecular imaging techniques cannot provide these important functionalities.

CHAPTER V

SUMMARY AND FUTURE WORK

This dissertation represents our effort to develop molecular contrast in coherence domain optical imaging. Three aims have been accomplished in this dissertation.

The first aim was to develop a pump-probe optical coherence microscopy. Currently high-resolution optical molecular imaging plays an important role in many research fields, such as biology and biomedical science. The prevailing high resolution optical molecular imaging modalities are based on fluorescence. These molecules need exogenous tags because of their poor intrinsic fluorescence. Pump-probe spectroscopy is well developed modality for measuring the spectrum and dynamic of molecular species which are poor fluorophores. Thus, we developed a PPOCM, which combines OCT with Pump-probe spectroscopy. This technique does not rely on fluorescent tags. We imaged melanin in human skin tissue with nodular melanoma via PPOCM. The results show a strong contrast between the melanotic and amelanotic regions. This technique can be potentially used for early diagnosis of melanoma and the mapping of tumor margins during excision. This technique also can be extended to any biological chromophore with a known absorption spectrum.

However, the imaging speed of the system is not fast enough as we used a translation stage to move the sample for scanning. One of the future work is to design a fast imaging system employing X-Y galvanometers to scan the beam in X and Y directions. In order to obtain 3-D images, we may use a microscope instead of an

objective to vary the imaging depth quickly. We could extend this application to image hemoglobin or other chromophores with known absorption spectrum.

If there are multiple chromophores PPOCM cannot differentiate them. We know that the ground state recovery time and transient absorption spectrum can be used to differentiate among multiple chromophores. In this dissertation, we differentiated two related chromophores via a SRPPOCM system.

We first developed an inexpensive method to generate two synchronized pump beams at different wavelengths. We can obtain an OCM image and two PPOCM images at two different pump wavelengths simultaneously through SRPPOCM. By applying a model we derived, we obtained a concentration map of one chromophore to the total chromophores. We tested this system on a red-black hair sample, and the results indicate that SRPPOCM can provide strong contrast between pheomelanin and eumelanin. This result is not available either in the scattering based OCM image or in one color pump-probe optical coherence microscopy. SRPPOCM can be used to obtain the relative concentration of pheomelanin or eumelanin and it can be potentially used as a clinical tool for diagnosing different progression stages of melanoma. This technique can also be extended to differentiate other related chromophores.

In this study, we obtained the parameters, a, b, and c from the literature which may not be very accurate. One way to address this issue is to obtain the parameters, a, b, and c experimentally. We could obtain these parameters by measuring pure pheomelanin and eumelanin samples.

In general, depth ambiguity is associated with SHOCT as the depth information is not clearly resolved by collecting the forward generated second harmonic signal. We performed a preliminary study to investigate the feasibility of collecting the backward generated second harmonic signal from non-centrosymmetric nanocrystals, $BaTiO_3$ using a SHOCT in Fourier domain. The preliminary result shows that backward generated second harmonic signal collection from nanocrystals is feasible; therefore, the correct depth information can be reported. The nanocrystals can be processed for specific labeling in biomedical applications to improve molecular contrast, while the current molecular imaging technique cannot provide these important functionalities.

For the future study, we need to characterize the system, SNR, resolutions, and the fall off. As described in previous section, the two spectrometers do not provide adequate fall-off in Fourier domain OCT. Thus, a better spectrometer is required to improve the sensitivity of the system. In addition, we need to add an X-Y galvanometer into the system for faster scanning. After optimizing the system, we could apply this technique to image some biological samples by labeling them with the nanocrystals.

REFERENCES

1. Y. Sun, W. L. Chen, S. J. Lin, S. H. Jee, Y. F. Chen, L. C. Lin, P. T. C. So, and C. Y. Dong, "Investigating mechanisms of collagen thermal denaturation by high resolution second-harmonic generation imaging," Biophysical Journal **91**, 2620-2625 (2006).

2. M. Skala, K. Riching, D. Bird, A. Gendron-Fitzpatrick, J. Eickhoff, K. Eliceiri, P. Keely, and N. Ramanujam, "*In vivo* multiphoton fluorescence lifetime imaging of protein-bound and free nicotinamide adenine dinucleotide in normal and precancerous epithelia," J. Biomed. Opt. **12**, (2007).

3. S. Gonzalez, and Z. Tannous, "Real-time, *in vivo* confocal reflectance microscopy of basal cell carcinoma," Journal of the American Academy of Dermatology **47**, 869-874 (2002).

4. D. E. Marra, A. Torres, C. F. Schanbacher, and S. Gonzalez, "Detection of residual basal cell carcinoma by *in vivo* confocal microscopy," Dermatologic Surgery **31**, 538-541 (2005).

5. P. Theer and W. Denk, "On the fundamental imaging-depth limit in two-photon microscopy," J. Opt. Soc. Am. A **23**, 3139-3149 (2006).

6. M. Fuller, S. H. Streger, R. K. Rothmel, B. J. Mailloux, J. A. Hall, T. C. Onstott, J. K. Fredrickson, D. L. Balkwill, and M. F. DeFlaun, "Development of a vital fluorescent staining method for monitoring bacterial transport in subsurface environments," Appl. Environ Microbiol. **66**, 4486-4496 (2000).

7. H. Wilson, B. Seligmann, and T. Chused, "Voltage-sensitive cyanine dye fluorescence signals in lymphocytes: plasma membrane and mitochondrial components," J Cell Physiol **125**, 61-71 (1985).

8. P. J. Campagnola, M.-d. Wei, A. Lewis, and L. M. Loew, "High resolution Nonlinear Optical Imaging of Live Cells by Second Harmonic Generation," Biophysical Journal **77**, 3341-3349 (1999).

9. D. Oron, D. Yelin, E. Tal, S. Raz, R. Fachima, and Y. Silberberg, "Depth-resolved structural imaging by third-harmonic generation microscopy," Journal of Structural Biology **147**, 3-11 (2004).

10. Y. Fu, H. F. Wang, R. Y. Shi, and J. X. Cheng, "Second harmonic and sum frequency generation imaging of fibrous astroglial filaments in ex vivo spinal tissues," Biophysical Journal **92**, 3251-3259 (2007).

11. Y. Jiang, I. Tomov, Y. Wang, Z. Chen, “High resolution second-harmonic optical coherence tomography of collagen in rat-tail tendon,” Opt. Lett. **29**(10), 1090 (2004)

12. A. Zumbusch, G. R. Holtom, and X. S. Xie, "Three-dimensional vibrational imaging by coherent anti-Stokes Raman scattering," Physical Review Letters **82**, 4142-4145 (1999).

13. C. L. Evans, X. S. Xie, “Coherent anti-stokes raman scattering microscopy: chemically selective imaging for biology and medicine," Annu. Rev. Anal. Chem. **1** , 883-909 (2008).

14. J. Fujimoto, S. De Silvestri, E. P. Ippen, C. A. Puliafito, R. Margolis, and A. Oseroff, "Femtosecond optical ranging in biological systems, " Opt. Lett. **11**, 150-152 (1986).

15. S. J. Riederer, "Current technical development of magnetic resonance imaging," IEEE Eng. Med. Biol. Mag.**19** (2000).

16. M. Born and E. Wolf, *Principles of Optics: Electromagnetic Theory of Propagation, Interference and Diffraction of Light* (Cambridge University Press, Cambridge, UK 1999).

17. A.F.Fercher, K.Mengedoht, and W. Werner, "Eye-length measurement by interferometry with partially coherent light," Opt. Lett. **13**, 186-188 (1988).

18. B. Bouma and G. Tearney, *Handbook of Optical Coherence Tomography* (Marcel Dekker, Inc., New York, 2002).

19. J.S. Schuman, C.A. Puliafito, J.G. Fujimoto, *Optical Coherence Tomography of Ocular Diseases* (Slack Inc., Thorofare, NJ, 2004).

20. J. A. Izatt, M. D. Kulkarni, H.-W. Wang, K. Kobayashi, M.V. Sivak, Jr., "Optical coherence tomography and microscopy in gastrointestinal tissues ," IEEE Journal Of Selected Topics in Quantum Electronics. **2**, 1017 (1996)

21. K. D. Rao, M. A. Choma, S. Yazdanfar, A. M. Rollins, and J. A. Izatt, "Molecular contrast in optical coherence tomography by use of a pump-probe technique, " Opt. Lett. **28**, 340-342 (2003).

22. D. Fu, T. Ye, T. E. Matthews, B. J. Chen, G. Yurtserver, and W. S. Warren, "High resolution *in vivo* imaging of blood vessels without labeling," Optics Letters **32**, 2641-2643 (2007).

23. D. Fu, T. Ye, T. E. Matthews, G. Yurtsever, and W. S. Warren, "Two-color, two-photon, and excited-state absorption microscopy," J. Biomed. Opt. **12**, 054004 (2007).

24. B. E. Applegate, and J. A. Izatt, "Molecular imaging of endogenous and exogenous molecular chromophores with ground state recovery pump-probe optical coherence tomography," Optics Express **14**, 9142-9155 (2006).

25. A. F. Fercher, C. K. Hitzenberger, G. Kamp, S.Y. El-Zaiat, “Measurement of intraocular distances by backscattering spectral interferometry,” Opt.Commun. **117**, 43-48 (1995).

26. M. Choma, M. Sarunic, C. Yang, and J. Izatt, "Sensitivity advantage of swept source and Fourier domain optical coherence tomography," Opt. Express **11**, 2183-2189 (2003).

27. Wolfgang Drexler, James G. Fujimoto, *Optical Coherence Tomography: Technology and Applications* (Springer, New York, 2008).

28. C. E. Crespo-Hernandez, B. Cohen, and B. Kohler, "Base stacking controls excited-state dynamics in A•T DNA," Nature **436**, 1141 (2005).

29. B. E. Applegate, C. Yang, and J. A. Izatt, "Theoretical comparison of the sensitivity of molecular contrast optical coherence tomography techniques," Optics Express **13**, 8146-8163 (2005).

30. A. L. Clark, A. Gillenwater, R. Alizadeh-Naderi, A. K. El-Naggar, and R. Richards-Kortum, "Detection and diagnosis of oral neoplasia with an optical coherence microscope," J Biomed Opt. **9**, 1271-1280 (2004).

31. M. Vincensi, M. d’Ischia, A. Napolitano, E. Procaccini, G. Riccio, G. Monfrecola, P. Santoianni, and G. Prota, "Phaeomelanin versus eumelanin as a chemical indicator of ultraviolet sensitivity in fair-skinned subjects at high risk for melanoma: a pilot study, " Melanoma Res. **8**, 53–58 (1998).

32. B. E. Applegate, C. Yang, and J. A. Izatt, "Theoretical comparison of the sensitivity of molecular contrast optical coherence tomography techniques," Optics Express **13**, 8146-8163 (2005).

33. C. J. R. Sheppard and M. Gu, "Image formation in two-photon fluorescence microscopy, " Optik **86**, 104–106 (1990).

34. C. Y. Dong, P. T. C. So, C. Buehler, and E. Gratton, "Spatial resolution in scanning pump-probe fluorescence microscopy," Optik (Stuttg.) **106**, 7–14 (1997).

35. Q. Wan, B. E. Applegate, "Multiphoton coherence domain molecular imaging with pump probe, optical coherence microscopy," Opt. Lett. 35, 532–534 (2010).

36. B. M. Hoeling, A. D. Fernandez, R. C. Haskell, E. Huang, W. R. Myers, D. C. Petersen, S. E. Ungersma, R. Wang, M. E. Williams, and S. E. Fraser, "An optical coherence microscope for 3-dimensional imaging in developmental biology," Opt. Express **6**, 136-146 (2000).

37 . J. Kantor, D. Zieve, "Melanoma,"
http://www.ncbi.nlm.nih.gov/pubmedhealth/PMH0001853/, accessed on Sep. 08, 2011.

38. American Cancer Society. *Cancer Facts & Figures 2010*. Atlanta: American Cancer Society; 2010,
http://www.cancer.org/acs/groups/content/@nho/documents/document/acspc-024113.pdf, accessed on Sep. 06, 2011.

39. B. A. Shoo, R. W. Sagebiel, M. Kashani-Sabet, "Discordance in the histopathologic diagnosis of melanoma at a melanoma referral center," J. Am. Acad. Dermatol. **62**, 751–756 (2010).

40. H.Ozeki, K. Wakamatsu, S. Ito, I. Ishiguro, "Chemical characterization of eumelanins with special emphasis on 5,6-dihydroxyindole-2-carboxylic acid content and molecular size**,** " Analytical **248,** 149–157 (1997).

41. M. R. Chedekel, "Photochemistry and photobiology of epidermal melanins," Photochemistry and Photobiology, **35**, 881 – 885 (1982).

42. M. R. Vincensi, M. d'Ischia, A. Napolitano, E. M. Procaccini, G. Riccio, G. Monfrecola, P. Santoianni, and G. Prota, "Phaeomelanin versus eumelanin as a chemical indicator of ultraviolet sensitivity in fair-skinned subjects at high risk for melanoma: a pilot study, " Melanoma Res. **8**, 53–58 (1998).

43. T. G. Salopek, K. Yamada, S. Ito, and K. Jimbow, "Dysplastic melanocytic nevi contain highlevels of pheomelanin—quantitative comparison of pheomelanin eumelanin levels between normal skin, common nevi, and dysplastic nevi, " Pigment Cell Res. **4**, 172–179 (1991).

44. K. Jimbow, S. K. Lee, M. G. King, H. Hara, H. Chen, J. Dakour, and H. Marusyk, "Melanin pigments and melanosomal proteins as differentiation markers unique to normal and neoplastic melanocytes, " J. Invest. Dermatol. **100**, S259–S268 (1993).

45. L. Chin, "The genetics of malignant melanoma: lessons from mouse and man, " Nat. Rev. Cancer **3**, 559–570 (2003).

46. T. E. Matthews, I. R. Piletic, M.A. Selim, M.J. Simpson, and W.S. Warren, "Pump-Probe Imaging Differentiates Melanoma from Melanocytic Nevi," Sci Transl Med. **3**, 71ra15(2011).

47. G. Zonios, A. Dimou, I. Bassukas, D. Galaris, A. Tsolakidis, E. Kaxiras, "Melanin absorption spectroscopy: a new method for noninvasive skin investigation and melanoma detection," J. Biomed. Opt. 13, 014017(2008).

48. M. R. Lee, J. A. Izatt, E.A. Swanson, D. Huang, J.S. Schumun, C.P. Lin, C.A. Puliafito, J.G. Fujimoto, "*Optical coherence tomography for ophthalmic imaging: new technique delivers micron-scale resolution* , " IEEE Eng. Med. Biol. Mag. **14**, 67 (1995).

49. D. Huang, E. A. Swanson, C. P. Lin, J. S. Schuman, W. G. Stinson, W. Chang, M. R. Hee, T. Flotte, K. Gregory, C. A. Puliafito, and J. G. Fujimoto, "Optical coherence tomography," Science **254,** 1178-1181 (1991)

50. M. J.A. de Dood, "Second-harmonic generation," experiment report (2006), users.uj.edu.pl/~ufdzierz/PracFot/SHG_Dood.pdf.

51. W.R. Zipfel, R.M. Williams, W.W. Webb, Nat. Biotechnol, "Nonlinear magic: multiphoton microscopy in the biosciences,"**21**, 1369-1377 (2003).

52. A. Zoumi, A. Yeh, B.J. Tromberg, "Imaging cells and extracellular matrix *in vivo* by using second-harmonic generation and two-photon excited fluorescence," Proc. Nat. Acad. Sci. **99**, 11014-11019 (2002).

53. P.J.A. Campagnola, C. Millard, M. Terasaki, P.E. Hoppe, J.C. Malone, W.A, Mohler, "Three-dimensional high resolution second-harmonic generation imaging of endogenous structural proteins in biological tissues," *Biophys. J*. **82**, 493-508 (2002).

54. D. A. Dombeck, K. A. Kasischke, H. D. Vishwasrao, M. Ingelsson, B. T. Hyman, and W. W. Webb, "Uniform polarity microtubule assemblies imaged in native brain tissue by second harmonic generation microscopy," Proc. Nat. Acad. Sc. **100**, 7081-7086 (2003).

55. R. Leitgeb, C. K. Hitzenberger, and A. F. Fercher, "Performance of fourier domain vs. time domain optical coherence tomography," Opt. Express **11**, 889-894 (2003).

56. M. V. Sarunic, B. E. Applegate, and J. A. Izatt, Spectral domain second harmonic optical coherence tomography, Opt. Lett. **30,** 2391-2393 (2005).

57. J. Su, I. V. Tomov, Y. Jiang, and Z. Chen, "High resolution frequency-domain second-harmonic optical coherence tomography," Appl. Opt. **46**, 1770-1775 (2007).

VITA

Name:	Qiujie Wan
Address:	Department of Biomedical Engineering
	5045 Emerging Technologies Building
	3120 TAMU
	College Station, TX 77843
Email Address:	qjwan@neo.tamu.edu
Education:	B.S., Electrical Engineering, Anhui University of Technology.
	M.S., Biomedical Engineering, Texas A&M University.